Submitted to ApJ: November 30, 2015
Preprint typeset using LaTeX style emulateapj v. 01/23/15

arXiv:1601.01690v1 [astro-ph.GA] 7 Jan 2016

A COMPREHENSIVE ARCHIVAL *CHANDRA* SEARCH FOR X-RAY EMISSION FROM ULTRACOMPACT DWARF GALAXIES

Viraj Pandya[1,2], John Mulchaey[2], and Jenny E. Greene[1]
[1]Department of Astrophysical Sciences, Peyton Hall, Princeton University, Princeton, NJ and
[2]The Observatories of the Carnegie Institution for Science, 813 Santa Barbara Street, Pasadena, CA 91101, USA

(Dated: January 11, 2016)
Submitted to ApJ: *November 30, 2015*

ABSTRACT

We present the first comprehensive archival study of the X-ray properties of ultracompact dwarf (UCD) galaxies, with the goal of identifying weakly-accreting central black holes in UCDs. Our study spans 578 UCDs distributed across thirteen different host systems, including clusters, groups, fossil groups, and isolated galaxies. Of the 336 spectroscopically-confirmed UCDs with usable archival *Chandra* imaging observations, 21 are X-ray-detected. Imposing a completeness limit of $L_X > 2 \times 10^{38}$ erg s^{-1}, the global X-ray detection fraction for the UCD population is $\sim 3\%$. Of the 21 X-ray-detected UCDs, seven show evidence of long-term X-ray time variability on the order of months to years. X-ray-detected UCDs tend to be more compact than non-X-ray-detected UCDs, and we find tentative evidence that the X-ray detection fraction increases with surface luminosity density and global stellar velocity dispersion. The X-ray emission of UCDs is fully consistent with arising from a population of low-mass X-ray binaries (LMXBs). In fact, there are fewer X-ray sources than expected using a naive extrapolation from globular clusters. Invoking the fundamental plane of black hole activity for SUCD1 near the Sombrero galaxy, for which archival *Jansky Very Large Array* imaging at 5 GHz is publicly available, we set an upper limit on the mass of a hypothetical central black hole in that UCD to be $\lesssim 10^5 M_\odot$. While the majority of our sources are likely LMXBs, we cannot rule out central black holes in some UCDs based on X-rays alone, and so we address the utility of follow-up radio observations to find weakly-accreting central black holes.

Keywords: accretion, galaxies: active, galaxies: dwarf, galaxies: supermassive black holes, X-rays: binaries, X-rays: galaxies

1. INTRODUCTION

The formation mechanisms and central black hole occupation fraction of ultracompact dwarf (UCD) galaxies are unknown. First discovered more than fifteen years ago in the nearby Fornax cluster (Hilker et al. 1999; Drinkwater et al. 2000; Phillipps et al. 2001), *Hubble Space Telescope* imaging and high-resolution spectroscopy have shown that UCDs are extremely dense stellar systems rather than merely unresolved foreground stars in our own Galaxy. Although numerous studies have established the distinctiveness of UCDs compared to considerably smaller and fainter globular clusters (GCs) and considerably larger and brighter dwarf elliptical (dE) galaxies (e.g., Drinkwater et al. 2003; Mieske et al. 2008b; Norris & Kannappan 2011; Brodie et al. 2011), the origin of UCDs is still not clear. There are thought to be two primary formation channels for UCDs: (1) the merging of several smaller star clusters that produces a supermassive star cluster, and (2) the tidal stripping of a larger galaxy that gives rise to a naked nucleus (e.g., Brodie et al. 2011; Norris et al. 2014).

One hint about the origin of UCDs comes from studying their dynamical masses. Interestingly, the more massive UCDs show evidence for higher dynamical mass-to-light ratios than those expected from stellar population modeling alone, suggesting that at least some UCDs host a large amount of "dark mass" (Haşegan et al. 2005; Mieske et al. 2008b, 2013). The most prominent explanations for this dark mass include a bottom-heavy IMF (Mieske & Kroupa 2008), a top-heavy IMF leading to excess stellar remnants (Dabringhausen et al. 2012), and supermassive black holes (SMBHs; Mieske et al. 2013).

Recently, Seth et al. (2014) presented evidence for a SMBH in M60-UCD1 that accounts for $\sim 10\%$ of the total mass of that UCD, based on dynamical modeling of spatially-resolved spectroscopy. The exciting detection of a SMBH via dynamical modeling motivates us to search for alternative evidence of central black holes in UCDs, in this case using accretion. X-rays provide one of the cleanest ways to identify accretion onto SMBHs because they are insensitive to dust and can probe the low bolometric Eddington ratio regime (e.g., Gallo et al. 2010; Miller et al. 2015).

Although the optical and UV (e.g., Mieske et al. 2008a) properties of UCDs have been systematically explored, X-rays from UCDs as a whole remain largely unexplored. A handful of UCD discovery papers report merely whether or not the newly-classified UCDs host an X-ray point source (e.g., the first bona fide X-ray-detected UCD was SUCD1 near the Sombrero galaxy; Hau et al. 2009). Phillipps et al. (2013) present an archival study of the X-ray properties of UCDs limited to Fornax alone, finding an X-ray detection fraction of $\sim 8\%$ (down to $L_X \approx 6 \times 10^{37}$ erg s^{-1}). In this paper, we present the first comprehensive archival search for X-rays from UCDs in a variety of host systems, with the goal of identifying accreting central black holes. As we will show, many archival observations are deep enough to also

Electronic address: vgpandya@princeton.edu

probe low-mass X-ray binaries (LMXBs), high-mass X-ray binaries (HMXBs), and ultra-luminous X-ray sources (ULXs).

This paper is organized as follows. In section 2, we describe our sample of UCDs and their physical properties. In section 3, we derive the X-ray properties of UCDs. In section 4, we present correlations between X-ray emission and physical properties, and address the origin of the X-ray emission. We discuss our results in section 5 and summarize in section 6. Appendix A gives the IDs of archival *Chandra* datasets used, Appendix B discusses borderline detections, Appendix C comments on UCDs in Perseus and NGC 3115, and Appendix D gives the optical properties and X-ray upper limits for non-X-ray-detected UCDs.

2. SAMPLE

In this section, we introduce our sample of UCDs and describe their optically-derived properties.

2.1. *Optically-Defined UCDs in the Literature*

We began our study by searching the literature for all samples of optically-defined UCDs. We find a total of 578 known UCDs distributed among thirteen different host systems and four different environment types (clusters, groups, fossil groups, and isolated galaxies).[1] Of those 578 UCDs, 195 are classified on the basis of their photometry alone, and so are considered UCD "candidates." It is likely that some of these 195 UCD candidates are actually background galaxies or foreground stars. The remaining 383 UCDs are spectroscopically-confirmed members of their respective host systems, and so can be considered bona fide UCDs.[2] To maximize the sample size considered in this work, we consider both candidate and spectroscopically-confirmed UCDs.

Although we do not attempt to homogenize the definition of UCDs across different studies, we have tried to limit our sample to objects that were unambiguously classified as UCDs in the original studies. The definition of an unambiguous UCD varies between different studies, and can depend on M_V, optical half-light radius ($r_{\rm hl}$), or a combination of the two. Typically, $M_V \lesssim -11$ mag and $r_{\rm hl} \gtrsim 10$ pc for an unambiguous UCD, but there are exceptions (e.g., Gregg et al. 2009; Brodie et al. 2011). The M_V distribution of our UCDs has mean -11.26 mag and standard deviation 0.97 mag. The $r_{\rm hl}$ distribution of our UCDs has mean 18.2 pc and standard deviation 14.9 pc, with the largest value being ~ 100 pc. Given that the boundary between GCs and faint UCDs is imprecisely defined, our sample size would greatly increase if we extended our study to encompass borderline objects (e.g., the ω Centauri-like objects described in Hilker 2011).

In Table 1, we organize the list of previous studies from which we initially drew our UCD samples and properties, as a function of UCD host system. Table 1 also shows how many UCDs in each host system have usable archival *Chandra* observations (see also subsection 3.1). In addition to Table 1, we also refer the reader to the following compilations of physical properties of compact stellar systems, including UCDs: Norris et al. (2014); Norris & Kannappan (2011); Forbes et al. (2013); Misgeld & Hilker (2011); Hilker (2011).

2.2. *The Physical Properties of UCDs*

We adopt the optically-derived physical properties of our UCDs from the literature (i.e., from one of the references given in Table 1). A substantial number of our UCDs do not have fundamental physical properties available. Here we briefly address the homogeneity of our literature-based physical properties.

Whenever possible, we adopt the global stellar velocity dispersion (σ) and $r_{\rm hl}$ from Mieske et al. (2008b) and Mieske et al. (2013), since they accounted for aperture- and seeing-related effects in a homogeneous way. Otherwise, we adopt the values from the original papers if available. Note that different studies used different structural models to derive sizes (Sersic, Nuker, or King profiles). In addition, we adopt the dynamical masses ($M_{\rm dyn}$), and dynamical mass-to-light ratios in the V band ($M_{\rm dyn}/L_{\rm V}$), derived by Mieske et al. (2013) and the original papers for ~ 50 UCDs. We verified that the $M_{\rm dyn}$ definitions used in different studies are indeed consistent with each other by recomputing the virial mass, which we estimate following Spitzer (1987) and Hilker et al. (2007): $M_{vir} \approx 9.75 \times \frac{r_{\rm hl}\sigma^2}{G}$.

3. X-RAY ANALYSIS

In this section, we describe all work related to deriving the X-ray properties of UCDs.

3.1. *Chandra X-ray Data Retrieval*

For each UCD, we used the *CIAO*[3] tasks `find_chandra_obsid` and `download_chandra_obsid` to search for archival ACIS[4] imaging (excluding grating, continuous clocking, and interleaved mode observations) with off-axis angle[5] $\theta < 10$ arcmin. Although there was no constraint on the depth of the *Chandra* data, the shortest exposure time for an individual observation is generally 5 ksec. The restriction on θ is crucial because the *Chandra* point spread function (PSF) is highly variable as a function of θ (and effective energy): the PSF starts to become elliptical at $\theta > 1.0$ arcmin, and as θ increases, the radius of a circular aperture needed to enclose 90% of the PSF also increases. If a point source has $\theta > 10$ arcmin, it will look like locally-enhanced background, have an artificially-extended structure, and is unlikely to be found by most detection algorithms[6].

After all observations were downloaded, we discarded any observations whose Validation and Verification (V&V) reports indicated severe problems. We then reprocessed every observation with the *CIAO* task

[1] Recently, Liu et al. (2015) presented a sample of several new UCDs around M87, M49, and M60 in Virgo (a small fraction of which are spectroscopically-confirmed). Although we do not include these new UCDs in our study, we do not expect our results to change if we did incorporate them.

[2] There are a few more host systems which contain mostly UCD candidates (no radial velocities) but which have no usable archival *Chandra* imaging (e.g., the Antlia cluster; Caso et al. 2013). We do not consider those systems here.

[3] The Chandra Interactive Analysis of Observations software provided by the Chandra X-ray Center (Fruscione et al. 2006).

[4] The Advanced CCD Imaging Spectrometer instrument.

[5] The off-axis angle is defined as the separation between the position of a source and the aim point of an observation.

[6] See section 4.2.3 of The *Chandra* Proposers' Observatory Guide: `http://cxc.harvard.edu/proposer/POG/html/chap4.html`

Table 1
UCD Sample

System (1)	N_{tot} (2)	N_{spec} (3)	$N_{chandra}$ (4)	References (5)
Centaurus	30	30	27	Mieske et al. (2007a, 2009)
Coma	87	41	35	Chiboucas et al. (2011); Madrid et al. (2010)
Fornax	78	78	62	Bergond et al. (2007); Firth et al. (2008); Gregg et al. (2009); Hilker et al. (2007); Mieske et al. (2008b, 2013)
HCG 22+90	21	21	21	Da Rocha et al. (2011)
Hydra	83	54	67	Misgeld et al. (2008, 2011); Wehner & Harris (2007)
NGC 1023	15	0	1	Mieske et al. (2007b)
NGC 1132	6	6	6	Madrid & Donzelli (2013); Madrid (2011)
NGC 3115	31	6	31	Jennings et al. (2014)
NGC 5128	27	27	23	Rejkuba et al. (2007); Mieske et al. (2008b, 2013); Peng et al. (2004); Martini & Ho (2004)
NGC 7252	1	1	1	Schweizer & Seitzer (1998); Fellhauer & Kroupa (2005); Maraston et al. (2004)
Perseus	84	14	28	Penny et al. (2012, 2014)
Sombrero	1	1	1	Hau et al. (2009)
Virgo	114	104	70	Brodie et al. (2011); Francis et al. (2012); Haşegan et al. (2005); Seth et al. (2014); Norris et al. (2014); Sandoval et al. (2015); Strader et al. (2013); Zhang et al. (2015); Evstigneeva et al. (2008, 2007); Paudel et al. (2010); Janz et al. (2015)
Total	578	383	373	–

Note. — References for the 13 UCD host systems probed in this paper as well as the number of UCDs in each host system satisfying our selection criteria. Col (1): UCD host system. Col (2): Total number of UCDs. Col (3): Total number of spectroscopically-confirmed UCDs. Col (4): Total number of UCDs with at least one usable Chandra observation. Col (5): References from which we drew our sample of UCDs.

`chandra_repro` to use the latest software and calibration updates (CALDB version 4.6.7). Forgoing astrometric corrections, we adopted the standard *Chandra* astrometric reference frame because it has an overall 90% absolute positional uncertainty of 0.6 arcsec, which is good enough for our purposes.

Table 1 gives the number of UCDs with at least one usable *Chandra* observation as a function of host system, and Appendix A gives the list of identifiers for all observations used in this work. We find that $373/578 \approx 65\%$ of UCDs have at least one usable *Chandra* observation.

3.2. *Detecting X-ray Counterparts*

We take a two-tiered approach to searching for X-ray point sources at the known optical positions of UCDs. The first tier involves the use of merged exposures (individually spanning several years) to gain the maximum possible sensitivity to faint sources. The second tier involves the use of the individual exposures to account for possible variable sources that may have been missed using the merged-observation approach.

3.2.1. *Tier I: Merged Observations*

The process of merging *Chandra* observations requires great care because of the significant degradation of the PSF at $\theta > 1$ arcmin and the non-uniformity of the PSF between different observations. Within most of the thirteen UCD host systems, there are typically several different observations, some of whose aim points can be separated by a few degrees. Combining such highly-separated observations into a single merged observation can contaminate point sources (from low-θ observations) with background counts (from high-θ observations), resulting in a noisy and artificially-extended source which is unlikely to be significantly detected. Therefore, we typically created multiple merged observations for each host system by separating individual observations into groups with similar aim points.

We chose to merge observations whose aim points were within 10 arcmin of each other for two reasons: (1) that is typically the maximum θ that a bright point source can have before it looks merely like locally-enhanced background, and (2) that was the search radius used to associate archival *Chandra* observations with each UCD. We accomplished this task using the machine learning k-means clustering algorithm which minimizes the sum of the distances from each observation's aim point to its assigned centroid position (there are k centroid positions initialized by the user) via an iterative procedure. This has the advantage that each UCD is then assigned to only one of the k merged images – the image whose k-means centroid position is closest to the UCD's own optical position.

We used the *CIAO* task `merge_obs` to combine the individual observations associated with each of the k groups, resulting in k merged images. No binning of the data was done so as to maintain the native resolution of *Chandra* (0.492 arcsec px^{-1}). For each of the merged images, we constructed a merged PSF map by doing an exposure map-weighted average of the individual contributing observations' PSF maps. The exposure map-weighted average accounts for significantly different exposure times and effective areas between the individual contributing observations.

On each of the k merged images, we ran the *CIAO* detection tool `wavdetect` in three different energy bands: full band (0.5-7.0 keV), soft band (0.5-2.0 keV), and hard band (2.0-7.0 keV). We used eight different wavelet scales (1, 2, 4, 8, 16, 24, 32, and 48 pixels), and required a significance threshold of 10^{-6} which corresponds to one false positive detection per *ACIS* CCD.

To cross-match the UCDs to the X-ray sources found by `wavdetect`, we adopted a circular matching radius of 1.5 arcsec. If a `wavdetect` X-ray source is found within 1.5 arcsec of a known UCD optical position, then that X-ray source is said to be coincident with the UCD. Although the optical radii of UCDs are typically less than one arcsec, our choice of 1.5 arcsec for the X-ray cross-matching radius helps to account for the instability and broadening of the *Chandra* PSF at $\theta > 1$ arcmin. We repeated this cross-matching for all three energy bands but we base our detection classifications on results in the full band. There were no instances of a source being detected in the hard and/or soft bands but not in the full band. We also did not have multiple unique X-ray sources cross-matched to a single UCD.

We found nineteen X-ray point sources coincident with the optical positions of UCDs using this merged-observation approach. The full-band postage stamps of these nineteen X-ray point sources are shown in Figure 1 and their optical properties are given in Table 3. In Appendix B, we discuss five borderline detections, while in

Appendix C we discuss non-detections in Perseus and NGC 3115.

3.2.2. *Tier II: Individual Observations*

While the first tier search is sensitive to very faint sources thanks to the significantly increased exposure times of merged observations, there are several instrumental and astrophysical effects that could conspire to give a non-detection in a merged image. During the first tier search, we assumed the following: (1) no intrinsic variability in a source, (2) no significant background variations among observations spanning more than ten years, and (3) no significant background contamination effects induced by merging observations whose aim points can be separated by up to 10 arcmin.

For the above reasons, we also carried out a search on the individual (non-merged) observations. For each host system, we first ran `wavdetect` on all individual observations in the same three energy bands (full, soft, and hard) and with the same parameters mentioned previously. We then cross-matched the UCDs to the X-ray point sources found in each individual observation and looked for new matches missed during the first tier. Of course, a UCD detected in a merged image may not be detected in every individual observation contributing to that merged image because the individual observations' exposure times (and the UCD's θ) may vary. In general, however, this unlocks time variability studies, which we will discuss in subsection 3.5.

We found two additional UCDs hosting X-ray point sources using this individual-observation approach: gregg45 in Fornax and HGHH92-C12=R281 in NGC 5128. Both gregg45 and HGHH92-C12=R281 were detected in only a single exposure. Their *Chandra* postage stamps are shown in Figure 1 and their optical properties are given in Table 3.

3.3. *Deriving X-ray Luminosities*

Since `wavdetect` is only a detection tool and not appropriate for X-ray photometry, here we describe our algorithm for deriving the flux and luminosity of each X-ray-detected UCD in the three energy bands (full, soft, and hard). There is neither a standard practice advocated by the Chandra X-ray Center nor a method widely adopted throughout the literature for deriving X-ray luminosities from a merged *Chandra* dataset. It is crucial that we derive X-ray luminosities using the merged datasets because most of our detections are based on the merged images.

For each X-ray-detected UCD, we extracted its spectrum from each of the individual observations used for its detection. We used the *CIAO* task `srcflux` which automatically defines a circular source aperture centered on the optical position of each UCD with the radius chosen to enclose 90% of the PSF (the radius depends on θ and the effective energy of the full-band: 2.3 keV). A background annulus is also automatically defined by `srcflux` with inner radius equal to the source aperture radius and outer radius equal to five times the source aperture radius.[7] `srcflux` automatically also applies PSF corrections to account for the fraction of counts falling outside the chosen source aperture by creating a circularly-symmetric PSF model at the UCD location using the task `arfcorr`.

We then did an exposure-weighted sum of the individual contributing observations' source and background region spectra, using the *CIAO* task `combine_spectra`. After computing the background-subtracted spectrum[8], we assumed an absorbed power-law spectral model with the absorption fixed to the Galactic value at the optical position of the UCD (Stark et al. 1992). In order to determine the best-fit photon index (γ) and normalization, we followed a two-step process.

First, since 11 of the 21 X-ray-detected UCDs have sufficiently high net counts (> 100 net counts) to do spectral fitting, we kept both γ and the normalization as free parameters for these 11 UCDs. We binned the spectra to ensure at least 15 counts in each energy bin. Using the Monte Carlo fitting algorithm (*moncar*) implemented in *Sherpa* (Freeman et al. 2001) along with the Gehrels (1986) χ^2 statistic, we found reasonable spectral fits; these are shown in Figure 2. We investigated the reason why $\chi^2_{\rm red} < 1$ for all fits as follows. For the five UCDs with > 300 net counts, we increased the minimum bin size from 15 to 40, 80, or 100 counts and re-fit the spectra. When the error per energy bin decreased due to the larger number of counts per bin, $\chi^2_{\rm red}$ indeed increased to ~ 1, but our fits did not significantly change. We settled on a bin size of 15 counts because some of our sources do not have enough counts to justify a bigger number and we want to apply a consistent bin size for all 11 sources. Altogether, $\chi^2_{\rm red}$ and visual inspection of the fits suggests that additional components beyond the fixed-absorption power law (e.g., soft X-ray thermal component or intrinsic absorption) are not necessarily justified.

For the remaining ten X-ray-detected UCDs, we fixed γ to 1.5 (the median of the best-fit values derived during the first iteration), and then we solved for the best-fit normalization using the same fitting approach described above. The flux and its 90% confidence interval in each of the three energy bands (full, soft, and hard) were derived by drawing 1000 random values from a Gaussian distribution with mean set to the best-fit model flux and standard deviation based on the uncertainty of that best-fit model flux. This was accomplished with the *Sherpa* task `sample_flux`. Finally, we converted the fluxes to luminosities with the luminosity-distance formula, assuming the distance to each UCD's host system (the distances are given in Table 3).

The X-ray properties of the X-ray-detected UCDs are given in Table 4.

[7] We visually inspected the source and background apertures in every individual observation associated with each X-ray-detected UCD. In some cases, there was a bright source nearby and so we manually resized or moved the background apertures to prevent contamination.

[8] The majority of our X-ray-detected UCDs' source regions have total (i.e., including the underlying background) counts $\gg 100$ so subtracting the background should be valid. In the remaining low-count cases, a standard practice advocated in the literature is to simultaneously fit the source and background spectra. However, modeling the *Chandra* X-ray background is not trivial, especially with few background counts, and we do not want to introduce additional systematic uncertainties. The crucial point is that, after subtracting the background for the few low-count UCDs, we do not end up in the (non-Poissonian) negative count case.

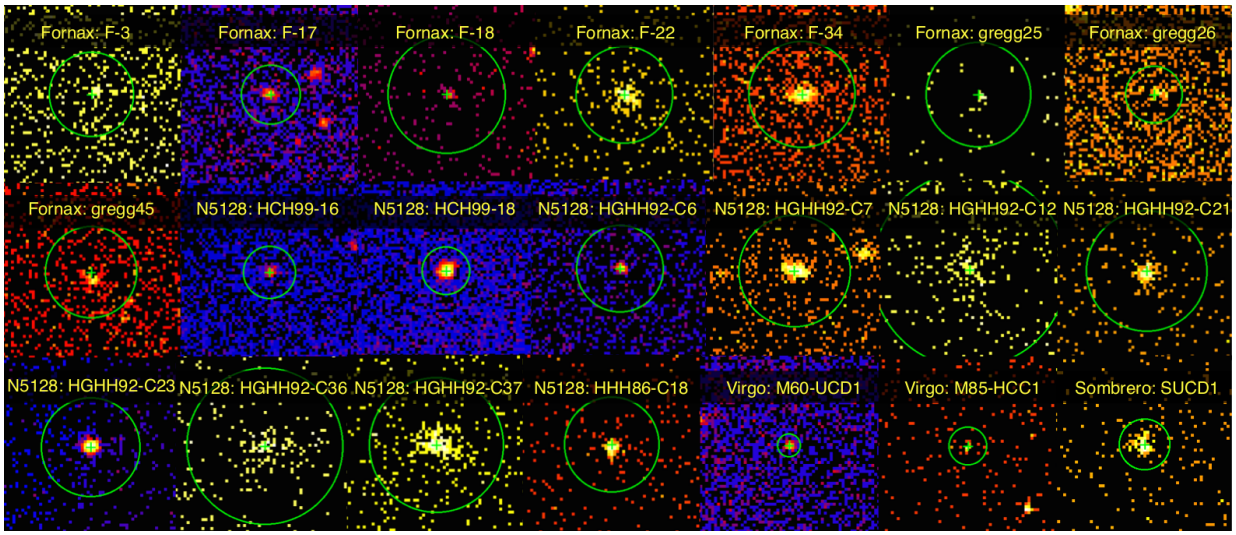

Figure 1. Approximately 30" × 30" postage stamps from the full band (0.5-7.0 keV) merged image for each of the 21 X-ray-detected UCDs. The green cross marks the optical position of each UCD. The green circle is the exposure time-weighted average of the circular apertures adopted to enclose 90% of the PSF in the individual observations (see subsection 3.3). The color-coding represents the count rate, where in each image blue is faintest, red is intermediate, and white is brightest.

3.4. *Deriving Upper Limits*

The majority of our UCDs are not directly detected by `wavdetect`, and so for those UCDs, we derive upper limits on the full-band (0.5-7.0 keV) flux and luminosity.[9] In many cases, we have extraordinarily deep imaging and can place an important constraint on X-ray emission from UCDs thought to host central BHs. However, defining and deriving upper limits is a highly non-trivial and controversial topic (e.g., Kashyap et al. 2010).

It is even more difficult in our case because we want to get the deepest possible upper limits by leveraging the summed exposure times of merged observations, but the individual contributing observations each have different effective exposures and aim points, and can span across more than 10 years. Tools such as WebPIMMS[10] are not appropriate because they make two assumptions that are generally flawed for large archival studies such as ours: (1) the source is perfectly on-axis, and (2) the sensitivity of ACIS for only one observing cycle is used. In practice, the source is not perfectly on-axis ($\theta > 0$ arcmin), and merged observations comprise datasets taken in many different observing cycles. Due to these complications, and because there is no standard algorithm recommended for deriving upper limits based on merged *Chandra* datasets, we describe our method in Appendix D. In short, we derived upper limits for the non-X-ray-detected UCDs by computing the number of net counts that would correspond to a local background fluctuation with Poisson probability 1%.

The optical properties and X-ray upper limits for non-X-ray-detected UCDs are given in Appendix D.

3.5. *X-ray Time Variability*

Many of our UCDs are covered in multiple archival observations spanning nearly fifteen years, and here we take advantage of that fact to search for time variability using the data products created during the X-ray luminosity derivation process (see subsection 3.3). We restrict the following time variability analysis only to X-ray-detected UCDs because we know that: (1) they are definitely X-ray emitters, and (2) they are securely detected in at least one archival observation. Individual archival observations in which an otherwise X-ray-detected UCD is not "re-detected" by `wavdetect` are still included in our analysis to test the possibility that the UCD's X-ray source "turned off." However, we discard any observations in which `srcflux` can only measure a 90% upper limit instead of a net count rate with 90% confidence bounds; this is typically a problem only for observations with exposure times $\lesssim 10$ ksec.

As is standard practice in active galactic nucleus (AGN) variability studies (e.g., Nandra et al. 1997; Ptak et al. 1998; Vaughan et al. 2003; Thornton et al. 2009; Young et al. 2012), we searched for variability in net count rate space rather than flux or luminosity space. Following Luo et al. (2013), we took a two-pronged approach to test for long-term X-ray time variability. First, we fit each UCD's "X-ray light curve" with a zero-slope straight-line model and computed $\chi^2_{\rm red}$. Second, we computed the maximal time variability indicator, $\sigma_{\rm max}$, based on the maximum difference between any two net count rates within a given UCD's light curve, normalized by their uncertainties (again, see Luo et al. 2013, and references therein):

$$\sigma_{\rm max} = {\rm max}_{\rm i,j} \frac{|R_i - R_j|}{\sqrt{\sigma^2_{R_i} + \sigma^2_{R_j}}} \ , \qquad (1)$$

where R_i and R_j are the net count rates in the ith and jth observations, and σ_{R_i} and σ_{R_j} are the uncertainties in those net count rates, respectively. The uncertainties σ_R include the contribution from the background and were derived using the Gehrels (1986) approximation.

[9] We did not derive upper limits for UCD candidates because: (1) all X-ray-detected UCDs are spectroscopically-confirmed, and (2) UCD candidates are not used when computing detection fractions or determining correlations.

[10] See `https://heasarc.gsfc.nasa.gov/docs/software/tools/pimms.html`.

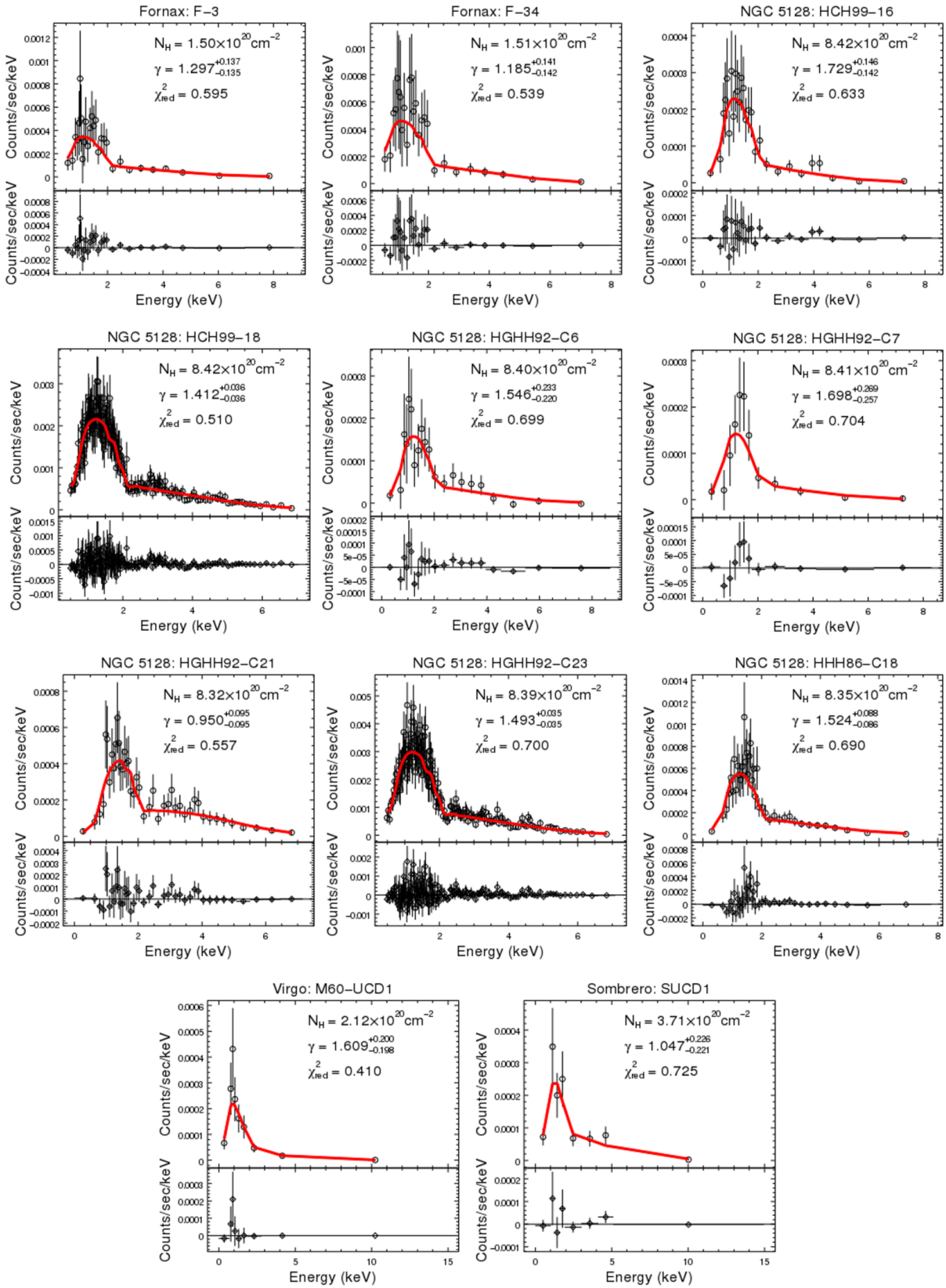

Figure 2. Spectra and best-fit models for the subset of our X-ray-detected UCDs with > 100 net counts. The best-fit photon index (γ) with 68% (1σ) confidence bounds, assumed Galactic absorption value in the direction of the UCD, and reduced χ^2 are shown in each subplot.

We present the results of the two approaches in Table 2. Adopting slightly more restrictive criteria than Luo et al. (2013), we consider a UCD to be a variability candidate if $\chi^2_{\rm red} \gtrsim 2$ and $\sigma_{\rm max} \gtrsim 3$. The following five UCDs clearly satisfy both criteria: F-17, HGHH92-C6, HGHH92-C7, HGHH92-C23, and HCH99-18. M60-UCD1 also exhibits evidence for variability, albeit with somewhat lower values of $\chi^2_{\rm red}$ and $\sigma_{\rm max}$. HGHH92-C21 is a borderline case due to a single spike in net count rate. The data suggest long-term variability on the order of months to years for these seven UCDs, and their median $\sigma_{\rm max} \approx 5.3$. Many of the non-variable UCDs have fewer observations available for characterizing their long-term variability as compared to the variable sources (see the $N_{\rm obs}$ column in Table 2), but their observations do span several years (with the exception of ~ 3 months for gregg25). The long-term X-ray light curves of the seven variability candidates and the non-variable SUCD1 are shown in Figure 3.

Lastly, we also looked for short-term variability (within a single observation – on the order of ksec) from each of the X-ray-detected UCDs using only observations in which the source region yielded > 50 net counts. First, we used the CIAO task `dither_region` to account for any time periods where our sources of interest were dithered over bad regions (off-chip, bad pixel, etc.) since that would induce artificial time variability due to instrumental effects. Then, we employed the *CIAO* task `glvary` which uses the Gregory & Loredo (1992) algorithm to: (1) slice an observation's event file into different time bins, and (2) look for significant deviations between the time-binned events. We did not find any compelling evidence for short-term time variability within any of the UCDs' observations.

Ideally, we would like to derive a characteristic long-term variability timescale and relate that to a hypothetical black hole mass. However, we do not have a sufficient number of data points in the light curves to detect a characteristic long-term variability timescale or amplitude. We also do not detect compelling evidence for short-term variability and thus cannot derive an estimate of, e.g., the crossing time, which directly probes the black hole mass (e.g., see section 2 of Peterson 2001). Nevertheless, the long-term variability of F-17, HGHH92-C6, HGHH92-C7, HGHH92-C21, HGHH92-C23, HCH99-18, and M60-UCD1 warrants further investigation.

4. ORIGIN OF THE X-RAY EMISSION

The most immediate conclusion to be drawn from our archival study is that across thirteen different host systems that collectively host 578 UCDs, we find only 21 X-ray-emitting UCDs (all coincidentally spectroscopically-confirmed). Considering only the 336 spectroscopically-confirmed UCDs with usable archival X-ray data and imposing a completeness limit of $L_X > 2 \times 10^{38}$ erg s^{-1} (to account for the variable depths in the different host systems), we measure a global X-ray detection fraction of $4/149 \approx 3\%$. In this section, we explore links between the X-ray and physical properties of UCDs with the goal of determining the origin of the X-ray emission.

4.1. *LMXBs versus Central Black Holes*

Our main concern is to quantify the expected contribution from the two most relevant sources of X-ray emission in UCDs: LMXBs (see discussion in subsection 4.4), and weakly-accreting central black holes (see discussion in subsection 5.2). Here, we briefly discuss the expected properties of the X-ray emission if dominated by one or the other.

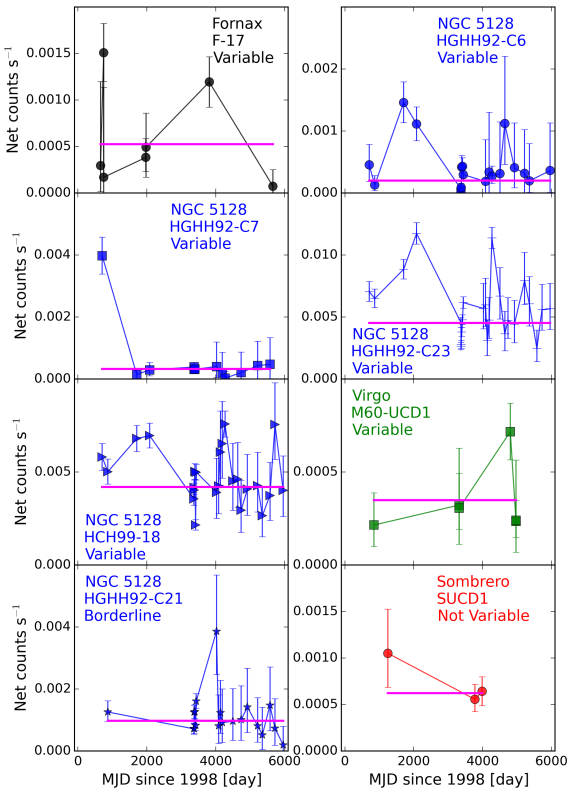

Figure 3. The long-term X-ray light curves for the seven variability candidates and the non-variable SUCD1. The modified Julian dates (MJD) shown are relative to the *Chandra*-specific reference MJD: MJD$_{ref}$ = 50814 days (January 1, 1998).

At luminosities below $\sim 5 \times 10^{38}$ erg s^{-1}, the LMXB X-ray luminosity function of GCs steeply rises (e.g., Fabbiano 2006; Kim et al. 2009)). Thus, our X-ray detections at these low L_X are likely dominated by accretion onto stellar-mass objects in LMXBs. At higher L_X, however, we can hope to be sensitive to accretion both onto central black holes and in LMXBs. For a given stellar mass, the LMXB fraction should rise with stellar density due to the increased probability of producing interacting stellar binaries (Jordán et al. 2004). In fact, as we will quantify in subsection 4.4, given the optical properties of the UCDs, we would expect many more LMXBs than our number of X-ray detections.

To estimate the likely emission from a central accreting black hole, consider that the Eddington luminosity[11] of a $10^6 M_\odot$ black hole is $\sim 1.3 \times 10^{44}$ erg s^{-1}.[12] Adopt-

[11] $L_{\rm edd} = 1.3 \times 10^{38} (M_{\rm BH}/M_\odot)$ erg s^{-1}.

[12] A $10^6 M_\odot$ black hole would account for $\sim 10\%$ of the typical UCD's dynamical mass, similar to the black hole mass fraction found in M60-UCD1 (Seth et al. 2014).

Table 2
Long-term X-ray Time Variability

UCD (1)	System (2)	N_{obs} (3)	σ_{max} (4)	χ^2_{red} (5)	Variable? (6)
F-17	Fornax	7	3.99	3.86	Yes
F-22	Fornax	4	1.20	0.56	No
F-34	Fornax	9	1.47	0.34	No
F-3	Fornax	3	0.88	0.40	No
F-18	Fornax	9	1.05	0.21	No
gregg25	Fornax	2	0.58	0.33	No
gregg26	Fornax	4	0.84	0.32	No
HGHH92-C6	NGC 5128	19	4.16	2.22	Yes
HGHH92-C7	NGC 5128	12	6.22	3.69	Yes
HHH86-C18	NGC 5128	21	1.77	0.51	No
HGHH92-C21	NGC 5128	19	3.04	1.16	Maybe
HGHH92-C23	NGC 5128	24	9.82	11.79	Yes
HGHH92-C36=R113	NGC 5128	4	0.24	0.03	No
HGHH92-C37=R116	NGC 5128	5	0.94	0.31	No
HCH99-16	NGC 5128	23	1.16	0.27	No
HCH99-18	NGC 5128	24	7.17	5.68	Yes
SUCD1	Sombrero	3	0.99	0.50	No
M60-UCD1	Virgo	6	2.54	1.52	Yes
HGHH92-C12=R281	NGC 5128	6	0.68	0.16	No
gregg45	Fornax	8	0.98	0.38	No

Note. — The long-term X-ray time variability properties of X-ray-detected UCDs with multiple observations. Col (1): UCD name. Col (2): UCD host system. Col (3): Number of individual observations in which `srcflux` could measure a net count rate with 90% confidence bounds (regardless of detection). Col (4): The maximal time variability indicator. Col (5): The reduced chi-squared from assuming a zero-slope straight-line fit model. Col (6): Whether we consider the UCD to exhibit long-term X-ray time variability.

ing the relation from Ho (2008) that $L_{bol} \approx 16 \times L_X$ for the typical low-luminosity AGN, our typical X-ray upper limits of 10^{37} and 10^{39} erg s^{-1} allow us to probe bolometric Eddington ratios ($\equiv L_{bol}/L_{edd}$) down to $\sim 7 \times 10^{-8}$ and $\sim 7 \times 10^{-6}$, respectively, assuming a $10^6 M_\odot$ central black hole. Given that the X-ray-detected M60-UCD1's dynamically-confirmed SMBH is radiating at $L_{bol}/L_{edd} \approx 4 \times 10^{-7}$, we certainly have the ability to detect some accreting central black holes if they exist.

The X-ray spectral and variability properties of UCDs can provide some additional clues about the nature of the X-ray emission. However, the median derived photon index (assuming an absorbed power law spectral model; $\gamma \approx 1.5$) is consistent with both a low-luminosity AGN (Ho 2008) and an LMXB in the hard/low state (Fabbiano 2006; Remillard & McClintock 2006). It is not clear what conditions would be required to produce the hard X-ray spectra ($\gamma \approx 1$) of some UCDs (F-34, HGHH92-C21, and SUCD1). In terms of variability, the greatest argument in favor of LMXBs would come from short-term variability which would imply short crossing times. Alas, we find no evidence for short-term variability (on the order of ksec), and instead detect only long-term variability (spanning years). Since the data do not suggest any periodicity, the variability could arise from either a central black hole or a population of LMXBs.

The X-ray properties alone are therefore inconclusive in addressing the possible domination of LMXBs over central black holes. In contrast, considering both the X-ray and optical properties together may help reveal concrete differences between the LMXB and central black hole scenarios.

4.2. *X-ray Detection Fraction*

We now ask whether the X-ray detection fraction depends on the physical properties of the UCDs. If the most massive and compact UCDs with the highest stellar velocity dispersions hosted either central accreting black holes (e.g., Mieske et al. 2013) or a large population of dark stellar remnants (e.g., Dabringhausen et al. 2012), then we would expect positive physical trends between the X-ray detection fraction and various physical properties. It is a bit complicated to address this vital question because we have such variable X-ray upper limits. Therefore, when computing the detection fraction at a given L_X completeness limit, we include all X-ray-detected UCDs (above that completeness limit) as well as non-X-ray-detected UCDs whose upper limits are greater than the completeness limit. We bin the detections as a function of four different physical properties: absolute V-band magnitude, dynamical mass-to-light ratio in the V band, global stellar velocity dispersion, and surface luminosity density ($\Sigma = \frac{L_V}{2\pi r_{hl}^2}$). As a concrete lower bound on the detection fraction upper limits, we also show the actual detection fraction in each bin (without including the non-X-ray-detected UCDs), assuming a completeness limit of $L_X > 10^{38}$ erg s^{-1}.

As can be seen in Figure 4, the upper limits on the detection fractions show an increasing trend between some bins for each measured property. However, the trends are not consistent for the different completeness limits that we explore, and they are also not consistent with the trends seen for the actual detection fractions assuming a completeness limit of $L_X > 10^{38}$ erg s^{-1}. More observations are needed, particularly at the high end of each physical property's distribution where the number of UCDs is lower. Tentatively, there does appear to be an increasing trend in the actual detection fractions (as-

Table 3
Optical Properties of X-ray-detected UCDs

UCD	System	RA	Dec	D	M_V	$\log(M/M_\odot)$	r_{hl}	v_{rad}	σ	M_{dyn}/L_V	n_{LMXB}	Ref
(1)	(2)	(3)	(4)	(5)	(6)	(7)	(8)	(9)	(10)	(11)	(12)	(13)
F-17	Fornax	54.64083	−35.43255	20.9	−11.37	6.8±5.8	3.46	1390.0	28.0±1.4	2.1±0.4	0.901	Mieske+13
F-22	Fornax	54.82375	−35.42503	20.9	−11.22	6.9±5.9	5.34	1054.0	29.1±1.5	3.2±0.9	0.290	Mieske+13
F-34	Fornax	54.55291	−35.48250	20.9	−10.83	6.3±5.6	4.19	1639.0	15.3±1.5	1.2±0.4	0.318	Mieske+13
F-3	Fornax	54.54333	−35.40172	20.9	−11.70	–	–	1626.0	31.3±1.5	–	–	Mieske+08a
F-18	Fornax	54.67500	−35.55361	20.9	−11.70	–	–	2024.0	19.1±1.4	–	–	Mieske+08a
gregg25	Fornax	54.55008	−35.66589	20.9	–	–	–	1307.0	–	–	–	Gregg+09
gregg26	Fornax	54.55937	−35.44550	20.9	–	–	–	1377.0	–	–	–	Gregg+09
gregg45*	Fornax	54.67975	−35.46708	20.9	–	–	–	1574.0	–	–	–	Gregg+09
HGHH92-C6	NGC 5128	201.34245	−43.04600	3.42	−11.01	6.5±5.7	4.3	854.5	20.7±1.5	1.5±0.4	0.369	Mieske+13
HGHH92-C7	NGC 5128	201.52254	−42.94233	3.42	−11.09	6.8±6.3	7.5	594.9	19.1	2.7	0.118	Mieske+08a
HHH86-C18	NGC 5128	201.41616	−43.08386	3.42	−10.14	6.2±5.7	3.2	479.8	14.7	0.9±0.3	0.264	Mieske+08a
HGHH92-C21	NGC 5128	201.46975	−43.09622	3.42	−10.39	6.7±6.2	7.0	461.3	17.2	3.9±1.4	0.062	Mieske+08a
HGHH92-C23	NGC 5128	201.47741	−42.99039	3.42	−11.66	6.8±6.3	3.3	673.7	29.5	1.7±0.6	1.393	Mieske+08a
HGHH92-C36=R113	NGC 5128	201.53220	−42.86675	3.42	−9.91	6.3±5.8	3.6	702.7	14.7	2.2±0.8	0.156	Mieske+08a
HGHH92-C37=R116	NGC 5128	201.54408	−42.89519	3.42	−9.83	6.0±5.6	3.3	611.7	12.0	1.5±0.5	0.173	Mieske+08a
HCH99-16	NGC 5128	201.37620	−42.99300	3.42	−10.08	6.3±5.8	12.1	458.2	8.4	2.2±0.8	0.013	Mieske+08a
HCH99-18	NGC 5128	201.38167	−43.00078	3.42	−11.38	7.0±6.6	13.7	455.0	18.7	3.7±1.4	0.043	Mieske+08a
HGHH92-C12=R281*	NGC 5128	201.27383	−43.17519	3.42	−10.52	6.63	10.8±1.4	440.4	13.1	3.1	0.027	Rejkuba+07
SUCD1	Sombrero	190.01304	−11.66786	9.95	−12.31	7.3	14.7±1.4	1293.1	25.0±5.6	3.0	0.106	Hau+09
M60-UCD1	Virgo	190.89990	11.53470	16.7	−14.20	8.3±7.5	24.2±0.5	1290.0	68±5	4.9±0.7	0.302	Strader+13
M85-HCC1	Virgo	186.34516	18.18158	16.7	−12.55	–	1.85±0.9	658.0	–	–	13.875	Sandoval+15

Notes: Col (1): UCD name adopted from the literature. ∗ means that the UCD was discovered during the second tier search using individual rather than merged observations. Col (2): UCD host system. Col (3): Optical right ascension of UCD [deg]. Col (4): Optical declination of UCD [deg]. Col (5): Distance adopted to UCD [Mpc]. Col (6): Absolute V-band magnitude [mag]. Col (7): $\log_{10}$ of (dynamical mass)/$M_\odot$. Col (8): Optical half-light radius [pc]. Col (9): Heliocentric radial velocity [km s^{-1}]. Col (10): Global stellar velocity dispersion [km s^{-1}]. Col (11): Dynamical mass-to-light ratio in the V-band [$M_\odot/L_\odot$]. Col (12): Expected number of LMXBs according to equation (17) of Sivakoff et al. (2007). Col (13): Primary reference for the UCD's optical properties.

Table 4
X-ray Properties of X-ray-detected UCDs

UCD (1)	System (2)	EXP (3)	θ (4)	s_x (5)	R (6)	NC_F (7)	NC_H (8)	NC_S (9)	F_F (10)	F_H (11)	F_S (12)	L_F (13)	L_H (14)	L_S (15)	HR (16)	γ (17)
F-17	Fornax	240	3.6	0.37	4.9	169.61±44.49	26.16±35.66	144.36±26.71	$-14.30^{+0.17}_{-0.27}$	$-14.44^{+0.35}_{-0.76}$	$-14.75^{+0.17}_{-0.30}$	$38.42^{+0.17}_{-0.27}$	$38.27^{+0.35}_{-0.76}$	$37.97^{+0.17}_{-0.30}$	−0.69	1.49
F-22	Fornax	93	5.3	0.59	8.0	126.79±42.60	29.12±35.56	99.67±23.60	$-14.05^{+0.20}_{-0.35}$	$-14.11^{+0.36}_{-0.94}$	$-14.50^{+0.18}_{-0.35}$	$38.67^{+0.20}_{-0.35}$	$38.61^{+0.36}_{-0.94}$	$38.22^{+0.18}_{-0.35}$	−0.55	1.49
F-34	Fornax	279	5.3	0.13	8.8	272.86±47.47	86.16±37.62	186.37±29.02	$-13.98^{+0.12}_{-0.17}$	$-14.11^{+0.21}_{-0.48}$	$-14.55^{+0.13}_{-0.19}$	$38.74^{+0.12}_{-0.17}$	$38.61^{+0.21}_{-0.48}$	$38.17^{+0.13}_{-0.19}$	−0.37	$1.19^{+0.14}_{-0.14}$
F-3	Fornax	414	4.5	0.89	7.0	288.53±47.85	92.87±37.84	195.32±29.36	$-14.15^{+0.11}_{-0.16}$	$-14.29^{+0.21}_{-0.49}$	$-14.68^{+0.13}_{-0.18}$	$38.56^{+0.11}_{-0.16}$	$38.42^{+0.21}_{-0.49}$	$38.04^{+0.13}_{-0.18}$	−0.36	$1.30^{+0.14}_{-0.14}$
F-18†	Fornax	204	5.5	0.51	9.7	32.87±43.22	0.96±36.98	31.92±22.46	$-14.68^{+0.36}_{-0.87}$	$-14.37^{+0.43}_{-1.00}$	$-15.11^{+0.39}_{-0.98}$	$38.04^{+0.36}_{-0.87}$	$38.35^{+0.43}_{-1.00}$	$37.61^{+0.39}_{-0.98}$	−0.94	1.49
gregg25†	Fornax	74	4.7	0.82	8.7	18.12±40.12	8.00±35.00	10.12±19.69	$-14.49^{+0.41}_{-1.04}$	$-14.05^{+0.42}_{-0.95}$	$-14.92^{+0.39}_{-0.91}$	$38.22^{+0.41}_{-1.04}$	$38.67^{+0.42}_{-0.95}$	$37.80^{+0.39}_{-0.91}$	−0.12	1.49
gregg26†	Fornax	194	2.7	1.21	4.7	5.99±40.20	1.00±34.78	4.91±20.25	$-15.31^{+0.44}_{-1.05}$	$-14.58^{+0.44}_{-1.01}$	$-15.74^{+0.44}_{-1.02}$	$37.41^{+0.44}_{-1.05}$	$38.14^{+0.44}_{-1.01}$	$36.97^{+0.44}_{-1.02}$	−0.66	1.49
gregg45*†	Fornax	265	4.8	1.49	7.6	45.20±41.89	4.00±35.17	41.04±22.83	$-14.87^{+0.34}_{-0.93}$	$-14.70^{+0.42}_{-1.04}$	$-15.31^{+0.39}_{-0.89}$	$37.85^{+0.34}_{-0.93}$	$38.02^{+0.42}_{-1.04}$	$37.41^{+0.39}_{-0.89}$	−0.82	1.49
HGHH92-C6	NGC 5128	612	4.4	0.35	7.2	175.11±46.02	67.95±38.24	108.00±25.70	$-14.61^{+0.18}_{-0.29}$	$-14.72^{+0.31}_{-0.86}$	$-15.09^{+0.19}_{-0.35}$	$36.53^{+0.18}_{-0.29}$	$36.42^{+0.31}_{-0.86}$	$36.06^{+0.19}_{-0.35}$	−0.23	$1.55^{+0.23}_{-0.22}$
HGHH92-C7	NGC 5128	445	5.4	0.45	9.2	106.16±43.32	30.37±36.21	76.71±23.89	$-14.70^{+0.24}_{-0.59}$	$-14.72^{+0.37}_{-1.05}$	$-15.13^{+0.25}_{-0.62}$	$36.45^{+0.24}_{-0.59}$	$36.42^{+0.37}_{-1.05}$	$36.02^{+0.25}_{-0.62}$	−0.43	$1.70^{+0.27}_{-0.26}$
HHH86-C18	NGC 5128	593	5.0	0.57	7.9	597.54±51.70	210.46±40.53	388.96±32.19	$-13.91^{+0.06}_{-0.07}$	$-14.08^{+0.12}_{-0.16}$	$-14.40^{+0.06}_{-0.08}$	$37.23^{+0.06}_{-0.07}$	$37.06^{+0.12}_{-0.16}$	$36.75^{+0.06}_{-0.08}$	−0.3	$1.52^{+0.09}_{-0.09}$
HGHH92-C21	NGC 5128	639	6.1	0.26	10.0	602.25±52.19	311.54±42.82	293.46±29.98	$-13.86^{+0.06}_{-0.07}$	$-13.95^{+0.10}_{-0.12}$	$-14.58^{+0.08}_{-0.09}$	$37.29^{+0.06}_{-0.07}$	$37.20^{+0.10}_{-0.12}$	$36.57^{+0.08}_{-0.09}$	0.03	$0.95^{+0.10}_{-0.10}$
HGHH92-C23	NGC 5128	652	5.1	0.20	8.2	3586.70±82.61	1312.04±57.91	2286.62±59.09	$-13.15^{+0.02}_{-0.02}$	$-13.31^{+0.03}_{-0.03}$	$-13.65^{+0.02}_{-0.02}$	$38.00^{+0.02}_{-0.02}$	$37.83^{+0.03}_{-0.03}$	$37.50^{+0.02}_{-0.02}$	−0.27	$1.49^{+0.04}_{-0.04}$
HGHH92-C36=R113	NGC 5128	106	7.1	–	12.9	69.42±41.41	5.67±35.09	64.75±22.12	$-14.05^{+0.25}_{-0.61}$	$-14.10^{+0.39}_{-0.94}$	$-14.56^{+0.27}_{-0.68}$	$37.09^{+0.25}_{-0.61}$	$37.05^{+0.39}_{-0.94}$	$36.59^{+0.27}_{-0.68}$	−0.84	1.49
HGHH92-C37=R116	NGC 5128	291	6.5	–	11.1	124.92±42.96	35.33±36.07	89.46±23.40	$-14.28^{+0.18}_{-0.37}$	$-14.39^{+0.32}_{-0.76}$	$-14.79^{+0.20}_{-0.40}$	$36.86^{+0.18}_{-0.37}$	$36.75^{+0.32}_{-0.76}$	$36.36^{+0.20}_{-0.40}$	−0.43	1.49
HCH99-16	NGC 5128	837	3.4	0.32	4.3	324.79±47.66	100.02±38.21	226.65±28.61	$-14.46^{+0.09}_{-0.12}$	$-14.68^{+0.24}_{-0.51}$	$-14.88^{+0.10}_{-0.14}$	$36.68^{+0.09}_{-0.12}$	$36.47^{+0.24}_{-0.51}$	$36.27^{+0.10}_{-0.14}$	−0.39	$1.73^{+0.15}_{-0.14}$
HCH99-18	NGC 5128	843	3.1	0.13	3.9	3386.95±81.37	1279.31±57.69	2119.43±57.56	$-13.26^{+0.02}_{-0.02}$	$-13.42^{+0.03}_{-0.03}$	$-13.79^{+0.02}_{-0.02}$	$37.88^{+0.02}_{-0.02}$	$37.73^{+0.03}_{-0.03}$	$37.35^{+0.02}_{-0.02}$	−0.25	$1.41^{+0.04}_{-0.04}$
HGHH92-C12=R281*	NGC 5128	216	8.2	1.43	16.2	69.48±42.24	25.31±36.06	44.04±22.08	$-14.50^{+0.31}_{-0.79}$	$-14.38^{+0.44}_{-0.95}$	$-15.01^{+0.34}_{-0.86}$	$36.64^{+0.31}_{-0.79}$	$36.76^{+0.44}_{-0.95}$	$36.13^{+0.34}_{-0.86}$	−0.27	1.49
SUCD1	Sombrero	192	3.1	0.29	4.2	106.37±41.99	48.12±36.01	59.21±21.72	$-14.17^{+0.25}_{-0.51}$	$-14.23^{+0.33}_{-0.88}$	$-14.79^{+0.23}_{-0.57}$	$37.90^{+0.25}_{-0.51}$	$37.85^{+0.33}_{-0.88}$	$37.28^{+0.23}_{-0.57}$	−0.1	$1.05^{+0.23}_{-0.22}$
M60-UCD1	Virgo	307	1.4	0.15	1.9	107.77±42.01	26.87±35.40	81.90±22.74	$-14.69^{+0.21}_{-0.46}$	$-14.62^{+0.42}_{-1.19}$	$-15.10^{+0.20}_{-0.41}$	$37.84^{+0.21}_{-0.46}$	$37.90^{+0.42}_{-1.19}$	$37.42^{+0.20}_{-0.41}$	−0.51	$1.61^{+0.20}_{-0.20}$
M85-HCC1†	Virgo	39	0.7	0.15	3.1	22.68±40.46	0.54±35.05	22.14±20.30	$-14.25^{+0.39}_{-0.95}$	$-14.02^{+0.43}_{-1.00}$	$-14.68^{+0.38}_{-0.94}$	$38.28^{+0.39}_{-0.95}$	$38.51^{+0.43}_{-1.00}$	$37.85^{+0.38}_{-0.94}$	−0.95	1.49

Notes: Col (1): UCD name adopted from the literature. ∗ means that X-ray emission from the UCD was detected during the second tier search using individual rather than merged observations. † indicates a borderline detection (net counts are consistent with zero); see Appendix B for more information. Col (2): UCD host system. Col (3): Total exposure time [ksec]. Col (4): Exposure time-weighted average off-axis angle of all observations used for flux derivation [arcmin]. Col (5): Separation between the optical position of the UCD and the center of the cross-matched X-ray source's aperture as defined by `wavdetect` [arcsec]. Col (6): Exposure time-weighted average radius of the circular apertures used to enclose 90% of the PSF in the individual observations [arcsec]. Col (7): Net counts in full band (0.5-7.0 keV) with 1σ Gehrels (1986) error [counts]. Col (8): Net counts in hard band (2.0-7.0 keV) with 1σ Gehrels (1986) error [counts]. Col (9): Net counts in soft band (0.5-2.0 keV) with 1σ Gehrels (1986) error [counts]. Col (10): Flux in full band with 90% confidence interval [erg s^{-1} cm^{-2}]. Col (11): Flux in hard band with 90% confidence interval [erg s^{-1} cm^{-2}]. Col (12): Flux in soft band with 90% confidence interval [erg s^{-1} cm^{-2}]. Col (13): Luminosity in full band with 90% confidence interval [erg s^{-1}]. Col (14): Luminosity in hard band with 90% confidence interval [erg s^{-1}]. Col (15): Luminosity in soft band with 90% confidence interval [erg s^{-1}]. Col (16): Classical hardness ratio: $(C_H - C_S)/(C_H + C_S)$. Col (17): Best-fit power law photon index (set to 1.49 – the median of the 11 derived indices – if γ was fixed due to $NC_F < 100$).

suming a completeness limit of $L_X > 10^{38}$ erg s^{-1}) toward higher bins of Σ and σ, which is also seen in the detection fraction upper limits. There is also a hint of environmental dependence in our raw detection fractions, which peak for the isolated galaxy NGC 5128. However, this dependence is driven entirely by the non-uniform X-ray sensitivities arising from the different host system distances. In the future, it would be very interesting to determine whether the accretion rate is in fact dependent on environmental richness and/or proximity to a massive neighboring galaxy (e.g., Liu et al. 2015).

4.3. *X-ray–Physical Correlations and Statistics*

Next, we search for: (1) correlations between L_X and physical properties within our sample of 21 X-ray-detected UCDs, and (2) statistical differences in the distributions of physical properties between the X-ray-detected and non-X-ray-detected samples. The results of these two searches can reveal clues about the origin of the X-ray emission. For example, a positive correlation between L_X and M_V would suggest a direct connection to the stellar, rather than dark, component of UCDs, and thus lend credence to LMXBs as the dominant source of the X-ray emission. On the other hand, a positive correlation between L_X and $M_{\rm dyn}/L_{\rm V}$ would suggest a connection to the dark component (of which central black holes are but one possibility; Mieske et al. 2013). Furthermore, if the $M_{\rm dyn}/L_{\rm V}$ distribution of the X-ray-detected sample is offset toward higher values than that of the non-X-ray-detected sample, then that would also suggest a relationship between the X-ray emission and the dark mass in UCDs.

The top panels of Figure 5 show the distribution of full-band (0.5-7.0 keV) L_X as a function of various physical properties: M_V, $M_{\rm dyn}/L_{\rm V}$, σ, and surface luminosity density (Σ). The L_X upper limits of non-X-ray-detected UCDs are shown via a two-dimensional histogram in the background. We see no obvious correlation between L_X and $M_{\rm dyn}/L_{\rm V}$ for the X-ray-detected UCDs. However, L_X appears to be negatively correlated with M_V and positively correlated with σ (i.e., optically brighter and thus more massive X-ray-detected UCDs, with higher stellar velocity dispersions, tend to also have higher L_X). To quantify the strength of the linear correlation between each property and $L_{X,0.5-7.0}$, we computed the Pearson product-moment correlation coefficient (R) and its corresponding p-value, given in Table 5. We excluded the outlier M60-UCD1 when computing R for M_V and σ, and we excluded the outlier M85-HCC1 when computing R for Σ. The values of R indicate a moderate positive correlation with σ at 99% significance, and a moderate negative correlation with M_V at 99% significance. The positive correlation with Σ is marginal (at $> 90\%$ significance). There is no correlation with $M_{\rm dyn}/L_{\rm V}$ ($p = 0.71$).

In the bottom panels of Figure 5, we compare the same four physical properties for spectroscopically-confirmed X-ray-detected and non-X-ray-detected UCDs[13]. From visual inspection alone, there are no systematic deviations between the two samples' distributions of M_V, $M_{\rm dyn}/L_{\rm V}$, and σ. However, there does appear to be a systematic offset between the surface luminosity density distributions: X-ray-detected UCDs tend to be more compact. We ran three different non-parametric tests to check for statistically-significant deviations between the two groups: the 2-sample Kolmogorov-Smirnov (KS) test, the Mann-Whitney-Wilcoxon (MWW) rank sums test, and the Anderson-Darling (AD) test. All three tests check whether two samples are consistent with being drawn from the same underlying parent population by making use of different test statistics. The number of X-ray-detected and non-X-ray-detected UCDs (with the required properties available) used for each test, and the resulting p-values, are given in Table 5. Only for the surface luminosity density Σ can we reject the null hypothesis that the X-ray-detected and non-X-ray-detected Σ distributions are drawn from the same parent populations, at the $> 99\%$ significance level ($p < 0.01$), suggesting an LMXB origin for the X-rays (consistent with Phillipps et al. 2013).

[13] We emphasize that most UCDs do not have these four physical properties available, so we must necessarily restrict comparisons to a small subset of the non-X-ray-detected UCDs. See Table 5.

Table 5
X-ray–Physical Statistics

Property	N_X	N_{non-X}	KS	MWW	AD	R (p)
M_V	18	130	0.923	0.808	0.854	-0.60 (0.01)
$M_{\rm dyn}/L_V$	15	37	0.292	0.207	0.287	0.11 (0.71)
σ	17	41	0.403	0.657	0.765	0.65 (0.01)
$L_V/(2\pi r_{\rm hl}^2)$	16	81	0.004	0.001	0.001	0.47 (0.08)

Note. — The p-values for each of the three non-parametric tests used to check whether the two samples of optical properties (X-ray-detected vs. non-X-ray-detected UCDs) are drawn from the same underlying parent population. The null hypothesis (that the two samples are drawn from the same underlying parent population) can only be rejected in the case of compactness, which shows statistical evidence for a discrepancy at the $> 99\%$ level. The Pearson product-moment correlation coefficient (R) and its corresponding p-value are also given to quantify the strength of each property's correlation with $L_{X,0.5-7.0}$.

4.4. *Contribution from LMXBs*

We now calculate the expected X-ray detection fraction from LMXBs alone. Note that HMXBs, which can have the same X-ray luminosities as LMXBs but which comprise O- and B-type stars, are not expected to contribute to the X-ray emission from UCDs' old stellar systems. Furthermore, since all of our X-ray-detected UCDs have peak $L_X < 10^{39}$ erg s^{-1}, they are by definition too faint to be ULXs (Fabbiano 2006). Our best means to estimate the LMXB rate in UCDs is to scale from GCs, for which far more is known. In GCs, as the stellar density increases, the LMXB rate per unit stellar mass also increases because of the higher probability of forming interacting stellar binaries (Jordán et al. 2004). The stellar encounter rate, Γ, scales as $M_*^{1.5} r_{\rm hl}^{-2.5}$ (see derivation in Dabringhausen et al. 2012). This relation is generally invoked to explain why the vast majority of LMXBs in the (local) Universe are found in GCs and only a small fraction are in dwarf and massive galaxies (e.g., Fabbiano 2006).

It is not yet known how UCDs fit into this picture since UCDs are far more compact than typical dwarf and massive galaxies, but less compact than GCs. Phillipps et al. (2013) noted that if the GC scaling relation were to be applied to UCDs, then the $\sim 10\times$ larger mass and size of UCDs would, in general, tend to cancel, giving rise to

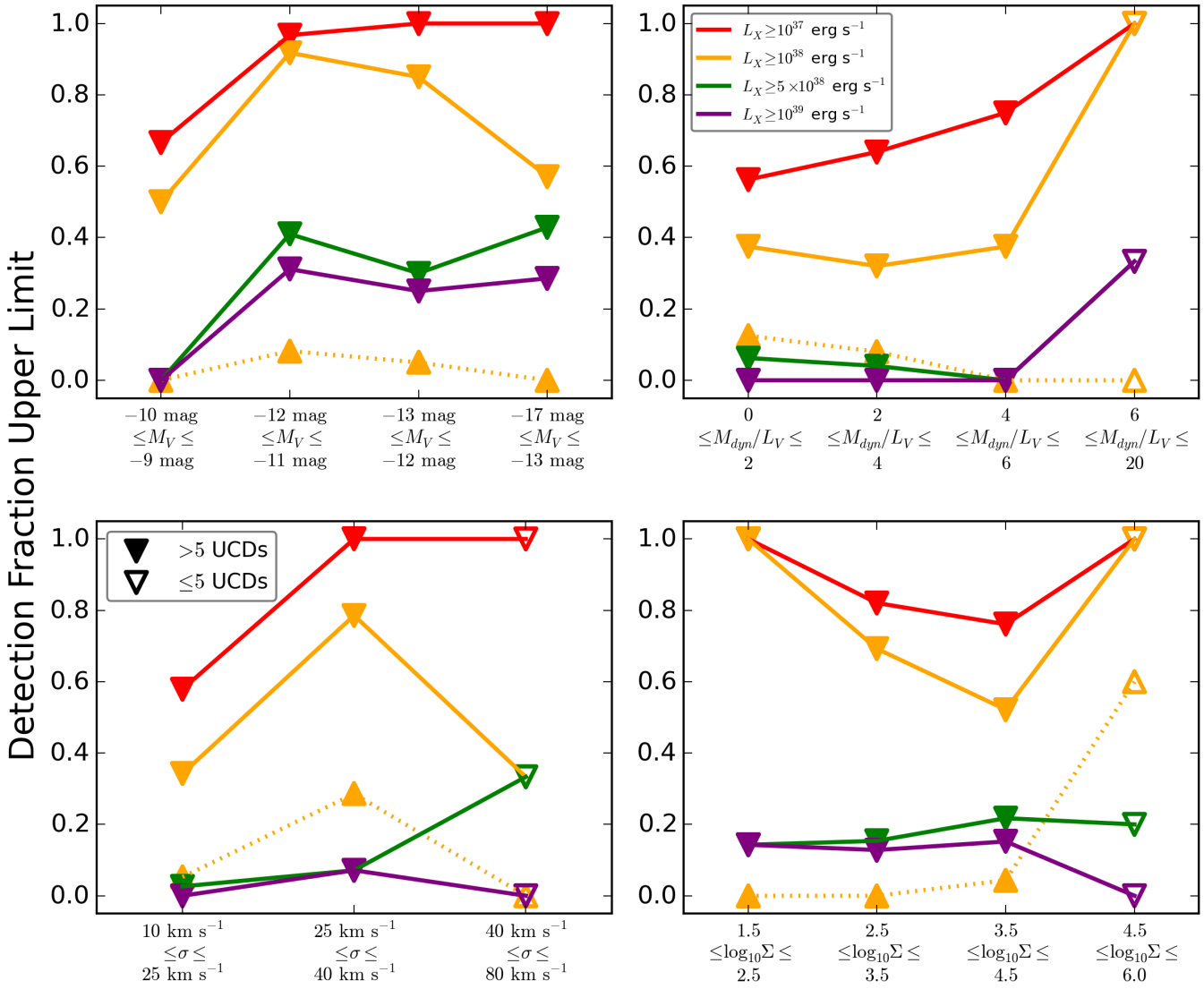

Figure 4. Upper limits on the X-ray detection fraction as a function of four different physical properties using four different L_X completeness limits. *Clockwise from top-left:* Absolute V-band magnitude, dynamical mass-to-light ratio in the V-band, the surface luminosity density in the V-band, and the global stellar velocity dispersion. Filled triangles are used for bins with more than 5 UCDs, and empty triangles are used for bins with 5 or fewer UCDs. Also included is a "lower bound" based on our actual detection fraction assuming a completeness limit of $L_X > 10^{38}$ erg s^{-1} (orange dotted lines and upward-facing triangles).

a similar LMXB detection fraction for UCDs as for GCs. The LMXB detection fraction among the entire GC population (without splitting into red (metal-rich) and blue (metal-poor) GC subpopulations) is $\sim$ 6.9% (down to $L_X \approx 2 \times 10^{37}$ erg s^{-1}; Kim et al. 2013). In contrast, the LMXB occurrence rate in non-nucleated massive galaxies is far lower than in nucleated dwarf galaxies and GCs, and the scaling relations for non-nucleated massive galaxies are derived with stellar mass rather than stellar density (e.g., Gilfanov 2004; Kim et al. 2006). At the moment, scaling to GCs is the best method that we have for obtaining a fiducial benchmark for UCDs, but the analogy is imperfect given their different star formation histories and stellar densities.

To quantify the occurrence of LMXBs in our sample of UCDs, we employ equation (17) of Sivakoff et al. (2007) which gives the expected number of LMXBs:

$$n_{\rm LMXB} = 8.0 \times 10^{-2} \left(\frac{M}{10^6 M_\odot}\right)^{1.237} 10^{0.90(g-z)} \left(\frac{r_{\rm hl}}{1\ {\rm pc}}\right)^{-2.22} . \quad (2)$$

Again, this scaling is not perfectly matched to our needs. Not only did Sivakoff et al. (2007) derive their equation (17) using GCs rather than UCDs, but they also used a luminosity-limited sample with a completeness limit of $L_X > 3.2 \times 10^{38}$ erg s^{-1}. Although we do not know $M_{\rm star}/L_V$ and $(g-z)$ for each individual UCD, we make the following educated guesses. We convert L_V to stellar mass assuming $M_{\rm star}/L_V = 4$ because UCDs in the literature have stellar mass-to-light ratios between 3 and 5. We assume $(g-z) = 1$ for all the UCDs based on the finding by Zhang et al. (2015) that UCDs around M87 in Virgo are tightly clustered around that value. Including the color/metallicity is important because blue (metal-poor) GCs are less likely to host an LMXB than are red

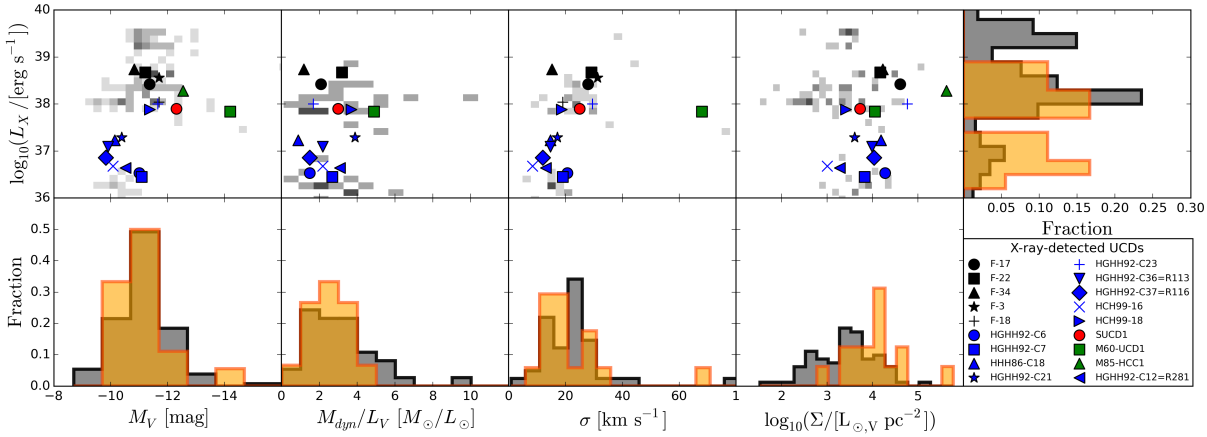

Figure 5. The distributions of full-band (0.5-7.0 keV) L_X and physical properties for our sample of 21 X-ray-detected UCDs. *Top row:* The L_X values plotted against four different physical properties: absolute V-band magnitude, dynamical mass-to-light ratio in the V-band, global stellar velocity dispersion, and surface luminosity density. The L_X upper limits for the non-X-ray-detected UCDs are shown as a two-dimensional histogram in the background. The right-most subplot shows the distribution of L_X itself: orange for X-ray-detected UCDs and gray for non-X-ray-detected UCDs. The UCDs in each host system are plotted with the same color: black (Fornax), blue (NGC 5128), red (Sombrero), and green (Virgo). *Bottom row:* The distribution of physical properties for spectroscopically-confirmed X-ray-detected (orange) and non-X-ray-detected (gray) UCDs. The total number of UCDs in both samples with the required measurements available is given in Table 5.

(metal-rich) GCs (e.g., Kim et al. 2013). Of the 16 X-ray-detected and 81 non-X-ray-detected UCDs with M_V and $r_{\rm hl}$ available, 21 non-X-ray-detected UCDs have upper limits greater than the Sivakoff et al. (2007) completeness limit, suggesting that we would not be sensitive to LMXBs with $L_X \approx 3.2 \times 10^{38}$ erg s^{-1} in those 21 UCDs. Thus, we calculate $n_{\rm LMXB}$ for the remaining 76 UCDs, and show $n_{\rm LMXB}$ for the 16 of these that are X-ray-detected in Table 3.

Taking a statistical approach (e.g., Gilfanov et al. 2004), when we sum the $n_{\rm LMXB}$ estimates for the 16 X-ray-detected UCDs as well as the 60 non-X-ray-detected UCDs with upper limits $< 3.2 \times 10^{38}$ erg s^{-1}, we expect ~ 25 LMXBs with $L_X > 3.2 \times 10^{38}$ erg s^{-1}. However, we have detected only 2 UCDs with $L_X > 3.2 \times 10^{38}$ erg s^{-1}. It is difficult to uniquely interpret this deficiency of detections (an excess of detections might have hinted at central black holes), but the most conservative interpretation is that LMXBs are responsible for the X-ray emission. The discrepancy between the expected 34% LMXB fraction and the actual 3% detection fraction reveals a difference between the bright ($L_X > 3.2 \times 10^{38}$ erg s^{-1}) ends of the GC-LMXB and UCD-LMXB X-ray luminosity functions (see subsection 5.1).

To sum up, our order of magnitude estimate for the expected number of LMXBs already suggests that all of the observed X-rays are consistent with coming from LMXBs. This conclusion is bolstered by the rising X-ray detection fraction with increasing surface luminosity density (Figure 4), and the tendency of X-ray-detected UCDs to be more compact than non-X-ray-detected UCDs (Figure 5). The X-ray spectra and long-term time variability are also consistent with LMXBs, as discussed in subsection 4.1. Taken together, our sample of X-ray-detected UCDs is compatible with a scenario in which LMXBs produce, and indeed dominate, the observed X-ray emission. The study of Phillipps et al. (2013), based on Fornax alone, came to similar conclusions.

5. DISCUSSION

5.1. *Deficiency of LMXBs in UCDs*

In subsection 4.4, we showed that the number of X-ray-detected UCDs is less than the expected number of LMXBs down to the L_X completeness limit of Sivakoff et al. (2007). Whereas we expected to detect ~ 25 UCDs with $L_X > 3.2 \times 10^{38}$ erg s^{-1}, we detected only two UCDs above that X-ray luminosity. The derivation of ~ 25 expected LMXBs was predicated upon the assumption that UCDs follow the same scaling relation as GCs between the number of LMXBs, the stellar density Γ, and other intrinsic properties such as color/metallicity. The deficiency of X-ray detections compared to the Sivakoff et al. (2007) prediction may be a clue that UCDs are not as efficient as GCs in producing LMXBs, even after controlling for stellar density. This lower LMXB production efficiency in UCDs may be the result of different metallicities, mean stellar ages, and/or structural properties as compared to GCs. In the future, it will be interesting to investigate whether this discrepancy holds at $L_X < 3.2 \times 10^{38}$ erg s^{-1}.

5.2. *UCD Central BH Occupation Fraction*

The original aim of this paper was to provide X-ray constraints on the central black hole occupation fraction of UCDs. However, any such X-ray constraints would be weak because, as an ensemble, UCDs are thought to host a large number of LMXBs whose collective X-ray emission may dominate over weakly-accreting central black holes, as shown in subsection 4.4. Unfortunately, even if a massive central black hole was present in a UCD, it may not necessarily be accreting, or it may be accreting below our detection limits.

We can address the detectability of weakly-accreting central black holes as follows. Suppose that all UCDs contain a central black hole with $M_{\rm BH}/M_{\rm star} = 10\%$, where $M_{\rm star}$ is derived from M_V as in subsection 4.4. By adopting such a high BH mass fraction (compared

to the $\sim 0.1\%$ seen in massive galaxies; e.g., Häring & Rix 2004), we will explore the region of parameter space that may be inhabited by extreme UCDs which are like M60-UCD1 and which may also host "overweight" central black holes (Seth et al. 2014; Sandoval et al. 2015). Our adopted BH mass fraction is also tantamount to assuming that all UCDs are tidally-stripped nuclei whose progenitors had $M_{\rm star} \sim 10^{10} M_{\odot}$. Of course, the dynamical modeling of Mieske et al. (2013) already suggests that only a small subset of UCDs host central black holes with $M_{\rm BH}/M_{\rm star} \gg 0.1\%$ (see also Seth et al. 2014). Nevertheless, estimated in this way, the median assumed $M_{\rm BH} \approx 10^6 M_{\odot}$ and the median assumed limiting $L_X/L_{\rm edd} \approx 5 \times 10^{-7}$.

A significant obstacle in our calculations is that we do not know a priori the true distribution of accretion rates, which we need in order to predict the X-ray luminosities corresponding to our assumed distribution of BH masses. Our best guess, perhaps, comes from the measurements of Miller et al. (2012), who find that $\sim 50\%$ of bulge-dominated galaxies with $M_{\rm star} \sim 10^{10} M_{\odot}$ are radiating at $L_X/L_{\rm edd} \geq 10^{-7}$. Since we are assuming that all UCDs are the tidally-stripped nuclei of more massive galaxies, we can use the population studied by Miller et al. (2012) as a proxy and consider the detectability of central black holes accreting at $L_X/L_{\rm edd} \geq 10^{-7}$. From our study, we would be sensitive to such weakly-accreting central black holes in 29 UCDs, all of which have an assumed limiting $L_X/L_{\rm edd} \leq 10^{-7}$. Presupposing that 50% of those 29 hypothetical central black holes are actually radiating at $L_X/L_{\rm edd} \geq 10^{-7}$ (based on Miller et al. 2012), we would expect to detect X-ray emission from roughly 14 central black holes. In fact, among the original 29 UCDs are 12 X-ray-detected UCDs, which is not so different from the expected number of 14 X-ray-detectable central black holes. However, since these 12 X-ray-detected UCDs all have $L_X \leq 10^{38}$ erg s^{-1}, we are again pushing into the faint LMXB-dominated X-ray regime and thus require complementary constraints from other types of measurements (e.g., optical emission-line spectroscopy and radio imaging).

5.3. *Complementary Radio Constraints*

Although LMXBs and central black holes are not mutually exclusive, we are hitting a limit in the effectiveness of X-ray observations to distinguish between the two scenarios. One hopeful way forward is to look at the ratio of radio to X-ray luminosity, which is a strongly increasing function of $M_{\rm BH}$. This so-called fundamental plane of black hole activity (e.g., Merloni et al. 2003; Plotkin et al. 2012) has been used to search for intermediate-mass black holes in GCs (e.g., Maccarone et al. 2005; Strader et al. 2012a,b; Chomiuk et al. 2013) and SMBHs in other local galaxies (e.g., Reines et al. 2011, 2014). It is beyond the scope of this paper to search for archival radio observations of all non-X-ray-detected UCDs. However, for the 21 X-ray-detected UCDs, we did search the VLA Data Archive[14] for serendipitous *Jansky Very Large Array* (*JVLA*) imaging at 1.4 GHz $< \nu <$ 10 GHz. Our search was restricted to the A- and B-array configurations, which provide the highest spatial resolution at 1.4 GHz $< \nu <$ 10 GHz. The high spatial resolution is important for distinguishing UCDs, which typically have sub-arcsec optical half-light radii, from nearby sources. Only three of the 21 X-ray-detected UCDs have archival *JVLA* imaging, and only one of those is public: observations of the Sombrero galaxy (Proposal 12B-007; PI: Zhiyuan Li).

SUCD1 is 2.84 arcmin from the primary beam center in a 2.5 hour integration at 5 GHz (C-band; single passband of width 2 GHz). Hau et al. (2009), who discovered SUCD1, noted the presence of off-center X-ray emission from archival *Chandra* observations, and claimed that the most likely origin of the X-ray emission is from LMXBs. Our study adds 176.2 ksec of new *Chandra* observations taken in 2008 and not considered in Hau et al. (2009). Although the additional *Chandra* imaging allows us to more finely constrain the X-ray properties of SUCD1, the archival *JVLA* imaging was taken ~ 4 years after the *Chandra* data, and so the two sets of observations may not track the same states of an accreting black hole, if one is present (e.g., Remillard & McClintock 2006). In Figure 6, we show the *HST* (optical), *Chandra* (hard X-ray), and *JVLA* (5 GHz) images of SUCD1. There is no 5 GHz signal at the optical position of SUCD1 whereas there is clearly hard X-ray emission. We measured the 5 GHz RMS within a circular aperture of radius 1 arcsec centered at the optical position of SUCD1 and found it to be 6.77 μJy. We adopted twice this RMS value as our upper limit on the 5 GHz flux density from SUCD1, and computed the corresponding upper limit on the 5 GHz radio luminosity: $L_{R,5} \lesssim 8.0 \times 10^{33}$ erg s^{-1}.

With our measured $L_{X,2-7}$ and upper limit on $L_{R,5}$ in hand, we can use the fundamental plane of black hole activity to estimate an upper limit for the mass of a central accreting black hole in SUCD1, assuming that one was present and that all of the hard X-ray emission is produced by that hypothetical object.[15] We arrive at an upper limit of $M_{\rm BH} \lesssim 10^5 M_{\odot}$, which would correspond to $\sim 0.5\%$ of the dynamical mass of SUCD1 and yield $L_{X,0.5-7.0}/L_{\rm edd} \approx 6 \times 10^{-6}$, assuming that all of the X-ray emission is produced by a central black hole.

Building on the constraint that we were able to place on SUCD1's hypothetical central black hole, we now examine the potential of a large-scale follow-up radio imaging campaign. Since X-ray constraints suggest that most UCDs have $M_{\rm BH}/M_{\rm star} < 10\%$, as discussed in subsection 5.2, let us suppose that, rather than LMXBs, the 21 X-ray-detected UCDs host central black holes with $M_{\rm BH}/M_{\rm star} = 0.1\%$. Assuming the fundamental plane of black hole activity, as in subsection 5.3, the predicted 5 GHz flux densities for X-ray-detected UCDs range from $\sim 1\mu$Jy to $\sim 37\mu$Jy, with a median of $\sim 3\mu$Jy. A similar calculation for the non-X-ray-detected UCDs, using their L_X upper limits, yields predicted 5 GHz flux density upper limits ranging from $\sim 0.2\mu$Jy to $\sim 8\mu$Jy, with a median of $\sim 1\mu$Jy. RMS levels of $\sim 2\mu$Jy and $\sim 1\mu$Jy can be achieved in ~ 3 hours and ~ 11 hours, respectively, with the *JVLA* in the A-configuration at 5 GHz (contrast this with the hundreds of hours worth of *Chandra* exposure time needed to reach the 10^{37} erg s^{-1} sensitivities presented in this paper). There are a handful

[14] `https://archive.nrao.edu/archive/advquery.jsp`

[15] From Merloni et al. (2003): $\log_{10} L_R = 0.60 \log_{10} L_X + 0.78 \log_{10} M_{\rm BH} + 7.33$, where L_R and L_X have units of erg s^{-1}.

of reasonably detectable UCDs assuming a 2μJy RMS level and a 3σ detection threshold. Several more radio-faint ($< 6\mu$Jy) UCDs become potentially detectable for $M_{\rm BH}/M_{\rm star} \approx 1\%$. Among them are M60-UCD1, M59-UCD3 and M59cO, the three most extreme UCDs in Virgo that are the targets of the other two existing, but proprietary, *JVLA* datasets (Proposal 15A-091, PI: Strader; Proposal 15A-154, PI: Mao). We have thus initiated a 5 GHz pilot radio survey of X-ray-detected UCDs in Fornax and NGC 5128 using the *JVLA* (Proposal 16A-382, PI: Pandya).

Although surveying individual UCDs may be prohibitive due to their faint 5 GHz emission, it would be interesting to consider a deep radio survey of the center of a nearby galaxy cluster (e.g., Virgo or Fornax). Then, an ~ 11 hour exposure could have many science goals, including a survey of radio emission from UCDs. Given that the primary beam width at 5 GHz is ~ 9 arcmin, targeting the center of Fornax (NGC 1399) would simultaneously observe 35/78 ($\approx 45\%$) Fornax UCDs, of which 6 are X-ray-detected. Targeting the center of Virgo (M87) would simultaneously observe 45/114 ($\approx 39\%$) Virgo UCDs, but there are no X-ray-detected UCDs around M87. In any case, by combining X-rays with deep radio imaging and extending our work on the prototypical SUCD1, we can hope to place a powerful constraint on the central (active) black hole occupation fraction of UCDs.

6. SUMMARY

In this paper, we have presented a comprehensive archival study of the X-ray properties of 578 UCDs distributed throughout thirteen different host systems, with the goal of finding weakly-accreting central black holes. Although we found 21 X-ray-detected UCDs with $L_{X,0.5-7.0}$ ranging from 2.8×10^{36} erg s^{-1} to 5.5×10^{38} erg s^{-1}, we showed that their X-ray emission is fully consistent with an origin in LMXBs. Interestingly, however, the number of X-ray detections in our ensemble of UCDs is far less than the expected number of LMXBs, and this deficiency of LMXBs in UCDs hints at a possible discrepancy between the formation histories of UCDs and GCs. Given that LMXBs and weakly-accreting central black holes are not necessarily mutually exclusive, we addressed the potential of a complementary radio study to augment the results of our archival X-ray study.

Our main conclusions are:

- Of the 336 spectroscopically-confirmed UCDs, 21 are X-ray-detected; imposing a completeness limit of $L_X > 2 \times 10^{38}$ erg s^{-1} to account for the variable depths of the different host systems, the global X-ray detection fraction is $4/149 \approx 3\%$.
- Seven of the 21 X-ray-detected UCDs show evidence of long-term X-ray time variability on the order of months to years.
- The X-ray emission from X-ray-detected UCDs is consistent with arising from a population of LMXBs.
- The number of X-ray detections, assuming an LMXB origin, is lower than we would expect based on the UCDs' stellar densities (using a naive extrapolation from GCs).
- SUCD1 near the Sombrero galaxy is detected at 2-7 keV with *Chandra* but not detected at 5 GHz with JVLA; assuming the fundamental plane of black hole activity, we place an upper limit on the mass of its hypothetical central black hole of $\lesssim 10^5 M_\odot$.
- A complementary archival or follow-up radio observing campaign may help identify weakly-accreting central black holes in UCDs via the fundamental plane of black hole activity.

ACKNOWLEDGEMENTS

We thank Zhiyuan Li for providing a fully-reduced *JVLA* image of Sombrero, Steffen Mieske for sending us the optical positions of UCDs in NGC 1023, and Andy Goulding for his suggestion to look at 4-7 keV images in Perseus. We are also grateful to the anonymous referee, the anonymous statistics expert, Michael Strauss, and Steffen Mieske for their thorough comments that improved the quality of this paper. In addition, VP greatly thanks: (1) Ken Glotfelty and Nicholas Lee at the *CXC Help Desk* for answering his questions about *Chandra* data manipulation, (2) Tony Perreault and Emmanuel Momjian at the NRAO Help Desk for their guidance on retrieving and analyzing archival *JVLA* data, and (3) Michael Strauss, in whose AST 303 course VP originally wrote a final paper describing the initial motivation for carrying out this work.

REFERENCES

Bergond, G., Athanassoula, E., Leon, S., et al. 2007, A&A, 464, L21
Brodie, J. P., Romanowsky, A. J., Strader, J., & Forbes, D. A. 2011, AJ, 142, 199
Caso, J. P., Bassino, L. P., Richtler, T., Smith Castelli, A. V., & Faifer, F. R. 2013, MNRAS, 430, 1088
Chiboucas, K., Tully, R. B., Marzke, R. O., et al. 2011, ApJ, 737, 86
Chomiuk, L., Strader, J., Maccarone, T. J., et al. 2013, ApJ, 777, 69
Da Rocha, C., Mieske, S., Georgiev, I. Y., et al. 2011, A&A, 525, A86
Dabringhausen, J., Kroupa, P., Pflamm-Altenburg, J., & Mieske, S. 2012, ApJ, 747, 72
Drinkwater, M. J., Gregg, M. D., Hilker, M., et al. 2003, Nature, 423, 519
Drinkwater, M. J., Jones, J. B., Gregg, M. D., & Phillipps, S. 2000, PASA, 17, 227
Evans, I. N., Primini, F. A., Glotfelty, K. J., et al. 2010, ApJS, 189, 37
Evstigneeva, E. A., Gregg, M. D., Drinkwater, M. J., & Hilker, M. 2007, AJ, 133, 1722
Evstigneeva, E. A., Drinkwater, M. J., Peng, C. Y., et al. 2008, AJ, 136, 461
Fabbiano, G. 2006, ARA&A, 44, 323
Fellhauer, M., & Kroupa, P. 2005, MNRAS, 359, 223
Firth, P., Drinkwater, M. J., & Karick, A. M. 2008, MNRAS, 389, 1539
Forbes, D. A., Pota, V., Usher, C., et al. 2013, MNRAS, 435, L6
Francis, K. J., Drinkwater, M. J., Chilingarian, I. V., Bolt, A. M., & Firth, P. 2012, MNRAS, 425, 325
Frank, M. J., Hilker, M., Mieske, S., et al. 2011, MNRAS, 414, L70
Freeman, P., Doe, S., & Siemiginowska, A. 2001, in Society of Photo-Optical Instrumentation Engineers (SPIE) Conference Series, Vol. 4477, Astronomical Data Analysis, ed. J.-L. Starck & F. D. Murtagh, 76–87

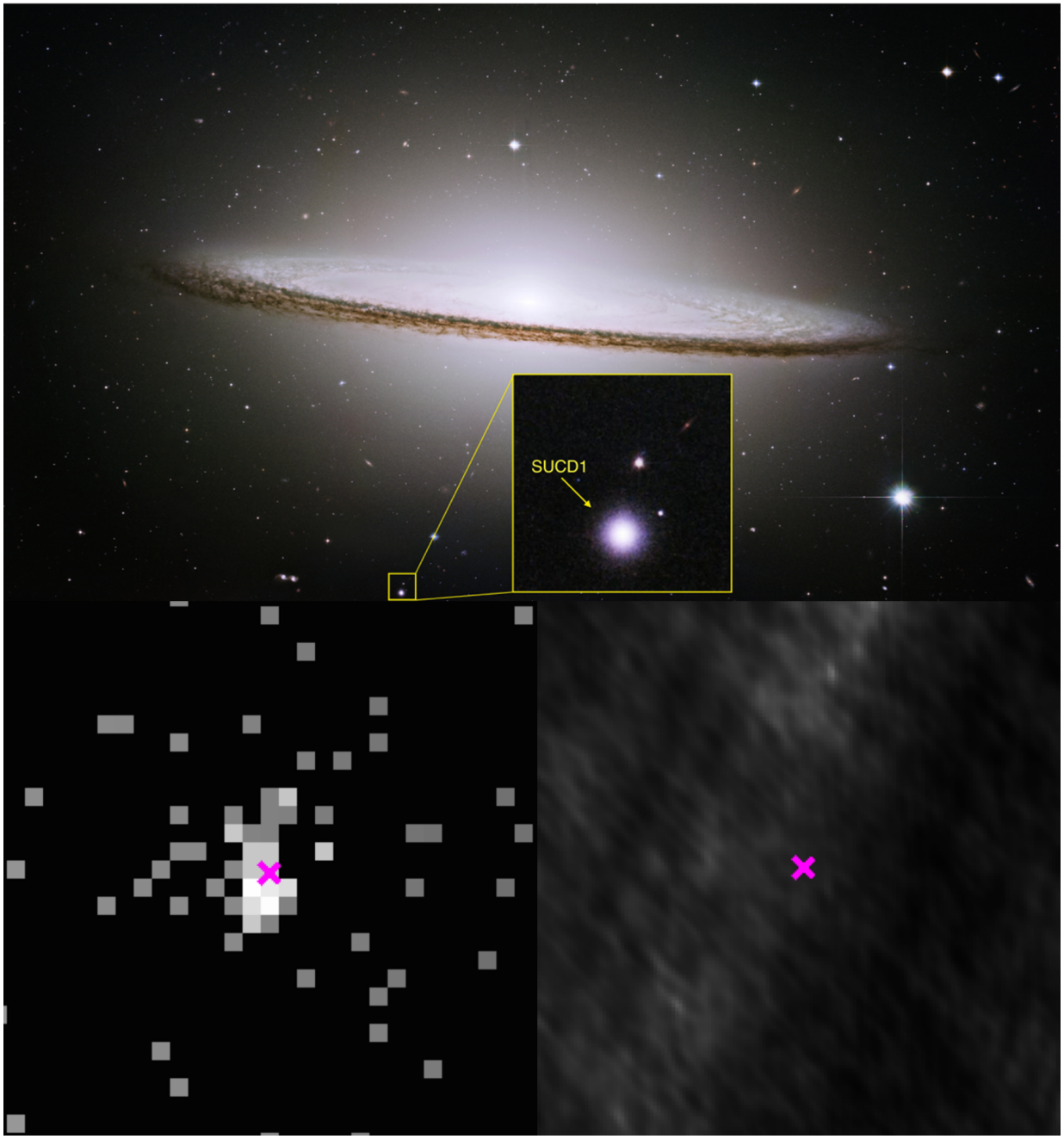

Figure 6. The multi-wavelength case study of SUCD1 near the Sombrero galaxy. *(Top)*: *HST/ACS* (*BVR*) image of Sombrero with SUCD1 identified via the 15" × 15" inset. *(Bottom left)*: Chandra hard band (2.0-7.0 keV) image (15" × 15") of SUCD1 showing a clear hard X-ray detection. *(Bottom right)*: JVLA A-configuration C-band (4-6 GHz) image (15" × 15") at location of SUCD1 showing a ~ 5 GHz non-detection. In both the Chandra and JVLA images, the magenta 'X' marks the optical position of SUCD1. *HST* image from NASA and The Hubble Heritage Team (STScI/AURA).

Fruscione, A., McDowell, J. C., Allen, G. E., et al. 2006, in Society of Photo-Optical Instrumentation Engineers (SPIE) Conference Series, Vol. 6270, Society of Photo-Optical Instrumentation Engineers (SPIE) Conference Series, 1
Gallo, E., Treu, T., Marshall, P. J., et al. 2010, ApJ, 714, 25
Gehrels, N. 1986, ApJ, 303, 336
Gilfanov, M. 2004, MNRAS, 349, 146
Gilfanov, M., Grimm, H.-J., & Sunyaev, R. 2004, MNRAS, 351, 1365
Gregg, M. D., Drinkwater, M. J., Evstigneeva, E., et al. 2009, AJ, 137, 498
Gregory, P. C., & Loredo, T. J. 1992, ApJ, 398, 146
Haşegan, M., Jordán, A., Côté, P., et al. 2005, ApJ, 627, 203
Häring, N., & Rix, H.-W. 2004, ApJL, 604, L89
Hau, G. K. T., Spitler, L. R., Forbes, D. A., et al. 2009, MNRAS, 394, L97
Hilker, M. 2011, in EAS Publications Series, Vol. 48, EAS Publications Series, ed. M. Koleva, P. Prugniel, & I. Vauglin, 219–224
Hilker, M., Baumgardt, H., Infante, L., et al. 2007, A&A, 463, 119
Hilker, M., Infante, L., & Richtler, T. 1999, A&AS, 138, 55
Ho, L. C. 2008, ARA&A, 46, 475
Janz, J., Forbes, D. A., Norris, M. A., et al. 2015, MNRAS, 449, 1716
Jennings, Z. G., Strader, J., Romanowsky, A. J., et al. 2014, AJ, 148, 32

Jordán, A., Côté, P., Ferrarese, L., et al. 2004, ApJ, 613, 279
Kashyap, V. L., van Dyk, D. A., Connors, A., et al. 2010, ApJ, 719, 900
Kim, D.-W., Fabbiano, G., Ivanova, N., et al. 2013, ApJ, 764, 98
Kim, D.-W., Fabbiano, G., Kalogera, V., et al. 2006, ApJ, 652, 1090
Kim, D.-W., Fabbiano, G., Brassington, N. J., et al. 2009, ApJ, 703, 829
Liu, C., Peng, E. W., Côté, P., et al. 2015, ApJ, 812, 34
Luo, B., Fabbiano, G., Strader, J., et al. 2013, ApJS, 204, 14
Maccarone, T. J., Fender, R. P., & Tzioumis, A. K. 2005, Ap&SS, 300, 239
Madrid, J. P. 2011, ApJL, 737, L13
Madrid, J. P., & Donzelli, C. J. 2013, ApJ, 770, 158
Madrid, J. P., Graham, A. W., Harris, W. E., et al. 2010, ApJ, 722, 1707
Maraston, C., Bastian, N., Saglia, R. P., et al. 2004, A&A, 416, 467
Martini, P., & Ho, L. C. 2004, ApJ, 610, 233
Merloni, A., Heinz, S., & di Matteo, T. 2003, MNRAS, 345, 1057
Mieske, S., Frank, M. J., Baumgardt, H., et al. 2013, A&A, 558, A14
Mieske, S., Hilker, M., Bomans, D. J., et al. 2008a, A&A, 489, 1023
Mieske, S., Hilker, M., Jordán, A., Infante, L., & Kissler-Patig, M. 2007a, A&A, 472, 111
Mieske, S., Hilker, M., Misgeld, I., et al. 2009, A&A, 498, 705
Mieske, S., & Kroupa, P. 2008, ApJ, 677, 276
Mieske, S., West, M. J., & de Oliveira, C. M. 2007b, in Groups of Galaxies in the Nearby Universe, ed. I. Saviane, V. D. Ivanov, & J. Borissova, 103
Mieske, S., Hilker, M., Jordán, A., et al. 2008b, A&A, 487, 921
Miller, B., Gallo, E., Treu, T., & Woo, J.-H. 2012, ApJ, 747, 57
Miller, B. P., Gallo, E., Greene, J. E., et al. 2015, ApJ, 799, 98
Misgeld, I., & Hilker, M. 2011, MNRAS, 414, 3699
Misgeld, I., Mieske, S., & Hilker, M. 2008, A&A, 486, 697
Misgeld, I., Mieske, S., Hilker, M., et al. 2011, A&A, 531, A4
Nandra, K., George, I. M., Mushotzky, R. F., Turner, T. J., & Yaqoob, T. 1997, ApJ, 476, 70
Norris, M. A., & Kannappan, S. J. 2011, MNRAS, 414, 739
Norris, M. A., Kannappan, S. J., Forbes, D. A., et al. 2014, MNRAS, 443, 1151
Paudel, S., Lisker, T., & Janz, J. 2010, ApJL, 724, L64
Peng, E. W., Ford, H. C., & Freeman, K. C. 2004, ApJS, 150, 367
Penny, S. J., Forbes, D. A., & Conselice, C. J. 2012, MNRAS, 422, 885
Penny, S. J., Forbes, D. A., Strader, J., et al. 2014, MNRAS, 439, 3808
Peterson, B. M. 2001, in Advanced Lectures on the Starburst-AGN, ed. I. Aretxaga, D. Kunth, & R. Mújica, 3
Phillipps, S., Drinkwater, M. J., Gregg, M. D., & Jones, J. B. 2001, ApJ, 560, 201
Phillipps, S., Young, A. J., Drinkwater, M. J., Gregg, M. D., & Karick, A. 2013, MNRAS, 433, 1444
Plotkin, R. M., Markoff, S., Kelly, B. C., Körding, E., & Anderson, S. F. 2012, MNRAS, 419, 267
Ptak, A., Yaqoob, T., Mushotzky, R., Serlemitsos, P., & Griffiths, R. 1998, ApJL, 501, L37
Reines, A. E., Plotkin, R. M., Russell, T. D., et al. 2014, ApJL, 787, L30
Reines, A. E., Sivakoff, G. R., Johnson, K. E., & Brogan, C. L. 2011, Nature, 470, 66
Rejkuba, M., Dubath, P., Minniti, D., & Meylan, G. 2007, A&A, 469, 147
Remillard, R. A., & McClintock, J. E. 2006, ARA&A, 44, 49
Sandoval, M. A., Vo, R. P., Romanowsky, A. J., et al. 2015, ApJL, 808, L32
Schweizer, F., & Seitzer, P. 1998, AJ, 116, 2206
Seth et al. 2014, Nature, 513, 398
Sivakoff, G. R., Jordán, A., Sarazin, C. L., et al. 2007, ApJ, 660, 1246
Spitzer, L. 1987, Dynamical evolution of globular clusters
Stark, A. A., Gammie, C. F., Wilson, R. W., et al. 1992, ApJS, 79, 77
Strader, J., Chomiuk, L., Maccarone, T. J., Miller-Jones, J. C. A., & Seth, A. C. 2012a, Nature, 490, 71
Strader, J., Chomiuk, L., Maccarone, T. J., et al. 2012b, ApJL, 750, L27
Strader, J., Seth, A. C., Forbes, D. A., et al. 2013, ApJL, 775, L6
Thornton, C. E., Barth, A. J., Ho, L. C., & Greene, J. E. 2009, ApJ, 705, 1196
Vaughan, S., Edelson, R., Warwick, R. S., & Uttley, P. 2003, MNRAS, 345, 1271
Wehner, E. M. H., & Harris, W. E. 2007, ApJL, 668, L35
Young, M., Brandt, W. N., Xue, Y. Q., et al. 2012, ApJ, 748, 124
Zhang, H.-X., Peng, E. W., Côté, P., et al. 2015, ApJ, 802, 30

APPENDIX

A. CHANDRA OBSERVATIONS USED

The following numbers refer to the Observation Identifiers ("ObsIDs") of unique *Chandra* datasets used in this work.

1. *Fornax cluster:* 14527, 239, 2942, 319, 320, 4168, 4169, 4170, 4171, 4172, 4173, 4174, 4176, 4177, 4742, 624, 9526, 9530, 9798, 9799

2. *Coma cluster:* 555, 556, 1086, 1112, 1113, 1114, 9714, 10672, 13993, 13994, 13995, 13996, 14406, 14410, 14411, 14415

3. *Perseus cluster:* 502, 503, 1513, 3209, 4289, 4946, 4947, 4948, 4949, 4950, 4951, 4952, 4953, 6139, 6145, 6146, 11713, 11714, 11715, 11716, 12025, 12033, 12036, 12037

4. *Virgo cluster:* 321, 322, 352, 517, 539, 785, 2016, 2068, 2072, 2707, 3717, 5826, 5827, 5828, 6186, 7210, 7211, 7212, 7864, 8046, 8047, 8050, 8057, 8058, 8063, 8064, 8071, 8074, 8078, 8079, 8090, 8094, 8095, 8098, 8103, 8107, 8109, 8110, 8127, 8131, 8182, 8507, 8581, 10241, 11274, 11783, 12888, 12889, 12975, 12976, 12978, 13985, 14328, 14358, 14359, 15178, 15179, 15180, 15757, 15758, 15759, 15760, 16033, 16260, 16261, 16585, 16586, 16587, 16590, 16591, 16592, 16593

5. *Hydra I cluster:* 2220

6. *Centaurus cluster:* 504, 505, 4190, 4191, 4954, 4955, 5310, 8179, 16223, 16224, 16225, 16534, 16607, 16608, 16609, 16610

7. *NGC 1132 fossil group:* 3576, 801

8. *NGC 1023 "poor" group:* 7131

9. *Hickson compact groups 22 and 90:* 8172, 905
10. *NGC 3115 galaxy:* 2040, 11268, 12095, 13817, 13819, 13820, 13821, 13822, 14383, 14384, 14419
11. *NGC 7252 galaxy:* 2980
12. *M104 (Sombrero) galaxy:* 1586, 9532, 9533
13. *Centaurus A (NGC 5128) galaxy:* 10722, 10723, 10724, 10725, 10726, 11846, 11847, 12155, 12156, 13303, 13304, 15294, 15295, 16276, 2978, 316, 3965, 7797, 7798, 7799, 7800, 8489, 8490, 962

B. BORDERLINE DETECTIONS

The following five UCDs present 0.5-7.0 keV (full band) net counts which are consistent with zero (i.e., the error bars are larger than the central value; see Table 4): F-18, gregg25, gregg26, gregg45, and M85-HCC1. Since `wavdetect` did find these sources to be significant (taking into account the spatial distribution of source and background region counts), we further scrutinized these UCDs' source and background regions in the individual contributing observations. Some of the UCDs required a redefinition of the background region due to contamination from a nearby bright source.

For F-18, gregg25, gregg45, and M85-HCC1, the total number of counts in the source region is greater than the number of local background counts by a factor of ~ 2. The net counts are also significantly greater than a fluctuation expected from the local background with Poisson probability 1% (between 1.5 to 2.75 times greater). Therefore, we consider these four UCDs to be bona fide X-ray-detected UCDs (although we note that they are all significantly off-axis).

For gregg26, the total counts and local background counts are 31 and 25 counts respectively, and so the margin of significance is very low. The net counts are also significantly less than a fluctuation expected from the local background with Poisson probability 1%: 5.98 compared to 12 counts. Visual inspection of its postage stamp in Figure 1 does suggest an over-density of counts above that seen in the local background. Since `wavdetect` found a significant detection for gregg26 taking into account the spatial distribution of the counts in the source and background apertures, we will continue to consider gregg26 an X-ray-detected UCD in what follows. Although including gregg26 does not affect the main results of our study, we do caution that its identification as an X-ray-emitting UCD is not completely secure.

C. COMMENTS ON PERSEUS AND NGC 3115

In both Perseus and NGC 3115, we have extraordinarily high exposure times, up to ~ 1.4 Msec and ~ 1.1 Msec respectively, but no unambiguous detections (among the 84 Perseus UCDs and 31 NGC 3115 UCDs). There are ~ 3 localized over-densities found by `wavdetect` in Perseus, each of which is within ~ 1.5 arcsec of a unique UCD. However, none of those appear to be genuine point sources and seem instead to arise from a knot of soft-X-ray-emitting hot gas. To further scrutinize those candidates, we created images in an even harder energy band that is presumably further devoid of emission from the thermally-emitting hot gas: 4-7 keV. With most of the thermal emission from the gas gone in these "harder-band" images and the lack of X-ray point sources near UCDs, we confirmed that there is no evidence in favor of X-ray-emitting UCDs in Perseus, including the extremely massive Perseus-UCD13.

Jennings et al. (2014) found that UCD20 in NGC 3115 is an X-ray emitter. We do find an X-ray point source near UCD20, but it is offset from the optical position of UCD20 by ~ 3.76 arcsec. Given that the 90% uncertainty on the absolute astrometry of the Chandra dataset is ~ 0.6 arcsec, that offset would correspond to a $\gtrsim 6\sigma$ positional error, which means that a match is unlikely. We compared the positions of the point sources in our merged image to known objects listed in the Chandra Source Catalog (Evans et al. 2010) and found excellent agreement. Therefore, we do not consider UCD20 to be an X-ray emitter.

D. OPTICAL PROPERTIES AND X-RAY UPPER LIMITS FOR NON-X-RAY-DETECTED UCDS

Here, we describe our derivation of upper limits for non-X-ray-detected UCDs. Just as for the X-ray-detected UCDs, we first extracted and combined the individual contributing observations' source and background region spectra for each non-X-ray-detected UCD using `srcflux` and `combine_spectra`. This extraction+combination step will also create the Auxiliary Response File (ARF) which gives the product of effective area (cm^2) and quantum efficiency (counts/photon) as a function of energy for a detector, and the ARF-weighted Redistribution Matrix File (RMF) which gives the response and finite resolution elements of the ACIS detectors used in the individual observations. These empirical exposure-weighted ARFs and RMFs yield more careful estimates of the count rate compared to the default, perfectly on-axis ACIS ARF and RMF assumed by tools such as WebPIMMS.

We next compute the scaled background counts, C_B, by multiplying the total counts observed in the background region by the ratio of source-to-background region areas, which is a standard practice to account for the fact that the background region is typically much larger than the source region. Then, we construct the inverse of the cumulative distribution function of the Poisson distribution characterized by mean C_B, and compute from that the total number of counts corresponding to the 99% tail of the function. We used the Python module `scipy.stats.poisson.ppf` for this task. The upper limit on net counts, $\mathcal{U}$, is thus defined as the total number of counts expected from such a fluctuation minus C_B. We consider the amplitude of this fluctuation above the local background, with Poisson probability 1%, to be the maximum possible number of net counts contributed by a source while still making that source indistinguishable from the local background (i.e., just barely non-detected at our adopted detection threshold).

As a sanity check, we verified that the net counts actually measured in a source region were lower than the $\mathcal{U}$ net counts calculated above assuming a Poisson fluctuation in the local background. This criterion was satisfied in nearly all cases. In the remaining few cases, we visually inspected the source and background regions to make sure that a detection was not hidden in the noise (which is what would be suggested if the actual net counts $> \mathcal{U}$). These cases typically occur in very high exposure time observations where there can be significant inhomogeneities in the local background (e.g., due to a knot of thermally-emitting hot gas). In some cases, we also had to redefine the background and/or source regions to avoid contamination or background over-subtraction due to a nearby point source. The crucial point is that we carefully checked all upper limits to ensure that there are no "missed" detections.

To go from units of net counts to flux, we first divide the $\mathcal{U}$ net counts by the summed exposure time, giving a net count rate. Then, we divide that net count rate by the product of the effective area and quantum efficiency which results in a photon flux.[16] Finally, we multiply that photon flux by the ARF-weighted mean energy per photon giving the conventional energy flux in units of [erg s^{-1} cm^{-2}]. Using the luminosity-distance formula with the assumed distance to the UCD's host system, we arrive at a luminosity in units of [erg s^{-1}].

[16] The value of the ARF at a given energy yields the product of the effective area and quantum efficiency. In low-count cases, it is prudent to use the ARF value at the ARF-weighted mean energy.

Table 6
Optical and X-ray Properties of Non-X-ray-detected UCDs

UCD	System	RA	Dec	D	M_V	log(M/M$_\odot$)	r$_{\rm hl}$	$v_{\rm rad}$	σ	M$_{dyn}$/L$_V$	EXP	θ	R	C$_{S+B}$	C$_B$	$\mathcal{U}$	F$_F$	L$_F$	Ref
(1)	(2)	(3)	(4)	(5)	(6)	(7)	(8)	(9)	(10)	(11)	(12)	(13)	(14)	(15)	(16)	(17)	(18)	(19)	(20)
f3_1	NGC 1023	38.41833	37.80639	12.25	–	–	–	–	–	–	–	–	–	–	–	–	–	–	Mieske+07b
f3_71	NGC 1023	38.51042	38.60917	12.25	–	–	–	–	–	–	–	–	–	–	–	–	–	–	Mieske+07b
f2_43	NGC 1023	38.55042	38.95472	12.25	–	–	–	–	–	–	–	–	–	–	–	–	–	–	Mieske+07b
f3_52	NGC 1023	38.69333	38.19083	12.25	–	–	–	–	–	–	–	–	–	–	–	–	–	–	Mieske+07b
f37	NGC 1023	38.74333	37.88222	12.25	–	–	–	–	–	–	–	–	–	–	–	–	–	–	Mieske+07b
f25	NGC 1023	38.75833	38.78278	12.25	–	–	–	–	–	–	–	–	–	–	–	–	–	–	Mieske+07b
f3_77	NGC 1023	38.94375	38.51389	12.25	–	–	–	–	–	–	–	–	–	–	–	–	–	–	Mieske+07b
f2_45	NGC 1023	38.94917	39.05611	12.25	–	–	–	–	–	–	4	9.4	20.4	0.0	1.3	3.7	< -13.7	<38.6	Mieske+07b
f2_51	NGC 1023	39.02833	39.30056	12.25	–	–	–	–	–	–	–	–	–	–	–	–	–	–	Mieske+07b
f2_56	NGC 1023	39.26333	39.43778	12.25	–	–	–	–	–	–	–	–	–	–	–	–	–	–	Mieske+07b
f2_53	NGC 1023	39.39417	39.20555	12.25	–	–	–	–	–	–	–	–	–	–	–	–	–	–	Mieske+07b
f1_20	NGC 1023	39.89792	39.43583	12.25	–	–	–	–	–	–	–	–	–	–	–	–	–	–	Mieske+07b
f46	NGC 1023	40.07375	37.88083	12.25	–	–	–	–	–	–	–	–	–	–	–	–	–	–	Mieske+07b
f49	NGC 1023	40.40750	37.79861	12.25	–	–	–	–	–	–	–	–	–	–	–	–	–	–	Mieske+07b
f4_23	NGC 1023	40.68250	38.09750	12.25	–	–	–	–	–	–	–	–	–	–	–	–	–	–	Mieske+07b
UCD1	NGC 1132	43.21250	−1.27194	99.5	–	–	77.1	7158.0	–	–	53	0.9	1.7	4.0	3.6	5.4	< -14.7	<39.4	Madrid+13
UCD6	NGC 1132	43.21250	−1.26833	99.5	–	–	9.9	7147.0	–	–	53	1.0	1.8	1.0	2.4	4.6	< -14.7	<39.4	Madrid+13
UCD4	NGC 1132	43.21667	−1.26194	99.5	–	–	16.7	6627.0	–	–	53	1.2	1.8	0.0	1.5	3.5	< -14.8	<39.2	Madrid+13
UCD2	NGC 1132	43.22500	−1.29417	99.5	–	–	13.3	6834.0	–	–	53	0.8	1.7	0.0	0.9	3.1	< -14.9	<39.2	Madrid+13
UCD5	NGC 1132	43.22917	−1.28861	99.5	–	–	13.0	6949.0	–	–	53	0.6	1.7	2.0	1.2	2.8	< -14.9	<39.1	Madrid+13
UCD3	NGC 1132	43.24583	−1.24833	99.5	–	–	19.8	7082.0	–	–	53	2.4	2.7	1.0	1.0	3.0	< -14.9	<39.1	Madrid+13
HCG22_UCD011	HCG 22+90	45.87537	−15.63583	33.1	–	–	–	2766.0	–	–	31	1.9	2.2	2.0	0.1	0.9	< -15.2	<37.9	DaRocha+11
HCG22_UCD010	HCG 22+90	45.88608	−15.64139	33.1	–	–	–	2755.0	–	–	31	1.3	1.8	0.0	0.3	1.7	< -14.9	<38.2	DaRocha+11
HCG22_UCD007	HCG 22+90	45.89267	−15.61756	33.1	–	–	–	2548.0	–	–	31	1.7	2.1	1.0	0.1	0.9	< -15.2	<37.9	DaRocha+11
HCG22_UCD001	HCG 22+90	45.89358	−15.61272	33.1	–	–	–	2834.0	–	–	31	2.0	2.3	1.0	0.1	0.9	< -15.2	<37.9	DaRocha+11
HCG22_UCD008	HCG 22+90	45.89600	−15.62525	33.1	–	–	–	2944.0	–	–	31	1.3	1.8	0.0	0.3	1.7	< -14.9	<38.2	DaRocha+11
HCG22_UCD002	HCG 22+90	45.90100	−15.62022	33.1	–	–	–	2552.0	–	–	31	1.4	1.9	0.0	0.6	2.4	< -14.8	<38.3	DaRocha+11
HCG22_UCD012	HCG 22+90	45.90133	−15.62106	33.1	–	–	–	2549.0	–	–	31	1.3	1.9	1.0	0.3	1.7	< -14.9	<38.2	DaRocha+11
HCG22_UCD016	HCG 22+90	45.90863	−15.62183	33.1	–	–	–	2487.0	–	–	31	1.2	1.9	0.0	0.5	2.5	< -14.8	<38.4	DaRocha+11
HCG22_UCD009	HCG 22+90	45.91479	−15.62717	33.1	–	–	–	2211.0	–	–	31	1.0	1.8	1.0	0.2	1.8	< -14.9	<38.2	DaRocha+11
HCG22_UCD015	HCG 22+90	45.91742	−15.61692	33.1	–	–	–	2789.0	–	–	31	1.6	2.1	0.0	0.3	1.7	< -14.9	<38.2	DaRocha+11
HCG22_UCD014	HCG 22+90	45.91896	−15.60519	33.1	–	–	–	2905.0	–	–	31	2.3	2.7	0.0	0.5	2.5	< -14.8	<38.3	DaRocha+11
HCG22_UCD006	HCG 22+90	45.91975	−15.62375	33.1	–	–	–	2654.0	–	–	31	1.3	1.9	0.0	0.1	0.9	< -15.2	<37.9	DaRocha+11
HCG22_UCD005	HCG 22+90	45.91996	−15.61586	33.1	–	–	–	2665.0	–	–	31	1.7	2.1	1.0	0.3	1.7	< -14.9	<38.2	DaRocha+11
HCG22_UCD003	HCG 22+90	45.93308	−15.62028	33.1	–	–	–	2652.0	–	–	31	2.0	2.3	1.0	0.1	0.9	< -15.2	<37.9	DaRocha+11
HCG22_UCD004	HCG 22+90	45.93592	−15.62872	33.1	–	–	–	2668.0	–	–	31	1.8	2.3	0.0	0.3	1.7	< -14.9	<38.2	DaRocha+11
HCG22_UCD013	HCG 22+90	45.93721	−15.61519	33.1	–	–	–	2646.0	–	–	31	2.3	2.7	1.0	0.3	1.7	< -14.9	<38.2	DaRocha+11
UCD60	Perseus	49.86792	41.57500	71.1	–	–	49.0	3735.0	–	–	1420	4.5	6.9	4215.0	4289.2	152.8	< -14.6	<39.2	Penny+12
UCD65	Perseus	49.88879	41.57619	71.1	–	–	13.6	7681.0	–	–	1368	4.4	6.7	4952.0	5118.8	167.2	< -14.5	<39.3	Penny+12
UCD1	Perseus	49.90683	41.49550	71.1	–	–	11.7	5717.0	–	–	1494	2.3	3.6	14554.0	14664.8	282.2	< -14.4	<39.4	Penny+12
UCD2	Perseus	49.91579	41.50478	71.1	–	–	26.9	5687.0	–	–	1494	2.7	3.7	21241.0	20989.0	338.0	< -14.3	<39.5	Penny+12
UCD7	Perseus	49.92096	41.53642	71.1	–	–	12.5	5272.0	–	–	1494	2.4	4.3	13676.0	13683.0	273.0	< -14.4	<39.4	Penny+12
UCD9	Perseus	49.92333	41.53553	71.1	–	–	14.4	9955.0	–	–	1494	2.4	4.3	14695.0	14592.9	282.1	< -14.4	<39.4	Penny+12
UCD13	Perseus	49.93804	41.53500	71.1	−12.81	8.36172783602	85.0	5292.0	38.0	19.85	1457	2.1	4.2	15919.0	16516.0	300.0	< -14.3	<39.5	Penny+12
UCD17	Perseus	49.95233	41.52161	71.1	–	–	18.4	5286.0	–	–	1457	2.5	4.3	28921.0	28362.5	392.5	< -14.2	<39.6	Penny+12
UCD19	Perseus	49.95817	41.52267	71.1	–	–	13.1	5680.0	–	–	1457	2.6	4.4	26781.0	27052.7	383.3	< -14.2	<39.6	Penny+12
UCD21	Perseus	49.95854	41.53581	71.1	–	–	31.2	5668.0	–	–	1402	2.8	4.8	20547.0	20440.0	333.0	< -14.3	<39.5	Penny+12
UCD23	Perseus	49.95896	41.48731	71.1	–	–	11.5	5693.0	–	–	1297	3.5	5.0	6668.0	6445.0	187.0	< -14.5	<39.3	Penny+12
UCD25	Perseus	49.96429	41.50481	71.1	–	–	11.5	4750.0	–	–	1297	3.1	4.4	17854.0	17893.0	312.0	< -14.3	<39.5	Penny+12
UCD29	Perseus	49.96996	41.50444	71.1	–	–	22.4	5250.0	–	–	1212	3.1	4.3	9949.0	10014.8	233.2	< -14.3	<39.4	Penny+12
UCD40	Perseus	49.99475	41.49864	71.1	–	–	13.9	5632.0	–	–	1139	3.9	5.6	4446.0	4580.3	157.7	< -14.5	<39.3	Penny+12

Notes: Upper limits were derived only for spectroscopically-confirmed UCDs, with the exception of NGC 3115 (which has $\sim$ 1.1 Msec of imaging) and NGC 1023 (which has no spectroscopically-confirmed UCDs). The UCDs are sorted by right ascension and declination so that all UCDs from the same host system are found in the same part of this table. Col (1): UCD name. Col (2): UCD host system. Col (3): UCD right ascension [deg]. Col (4): UCD declination [deg]. Col (5): Host system distance [Mpc]. Col (6): Absolute magnitude in V-band. Col (7): log$_{10}$ of (dynamical mass)/$M_\odot$. Col (8): Half-light radius [pc]. Col (9): Radial velocity [km s^{-1}]. Col (10): Global stellar velocity dispersion [km s^{-1}]. Col (11): Dynamical mass-to-light ratio in the V-band. Col (12): Total *Chandra* exposure time [ksec]. Col (13): Exposure time-weighted average off-axis angle of all observations used to derive upper limit [arcmin]. Col (14): Exposure time-weighted average radius of the circular apertures used to enclose 90% of the PSF in the individual observations [arcsec]. Col (15): Total counts in the source region [counts]. Col (16): Scaled background counts in the background region [counts]. Col (17): Number of counts expected from a fluctuation in the local background with Poisson probability 1% [counts]. Col (18): log$_{10}$ of 0.5-7.0 keV flux upper limit based on $\mathcal{U}$ counts [erg s^{-1} cm^{-2}]. Col (19): log$_{10}$ of 0.5-7.0 keV luminosity upper limit based on $mathcalU$ counts [erg s^{-1}]. Col (20): Primary reference paper for UCD's optical properties. *The full version of this table is available online.*